



HAL
open science

On the use of graph centralities to compute generalized inverse of singular finite element operators: applications to the analysis of floating substructures

Christophe Bovet

► To cite this version:

Christophe Bovet. On the use of graph centralities to compute generalized inverse of singular finite element operators: applications to the analysis of floating substructures. *International Journal for Numerical Methods in Engineering*, 2022, 124 (9), pp.1933-1964. 10.1002/nme.7193 . hal-03660559v3

HAL Id: hal-03660559

<https://hal.science/hal-03660559v3>

Submitted on 18 Jan 2023

HAL is a multi-disciplinary open access archive for the deposit and dissemination of scientific research documents, whether they are published or not. The documents may come from teaching and research institutions in France or abroad, or from public or private research centers.

L'archive ouverte pluridisciplinaire **HAL**, est destinée au dépôt et à la diffusion de documents scientifiques de niveau recherche, publiés ou non, émanant des établissements d'enseignement et de recherche français ou étrangers, des laboratoires publics ou privés.



Distributed under a Creative Commons Attribution - NonCommercial - NoDerivatives 4.0 International License

On the use of graph centralities to compute generalized inverse of singular finite element operators: Applications to the analysis of floating substructures

Christophe Bovet 

DMAS, ONERA, Université Paris Saclay,
Châtillon, F-92322, France

Correspondence

Christophe Bovet, DMAS, ONERA,
Université Paris Saclay, F-92322 Châtillon,
France.

Email: christophe.bovet@onera.fr

Summary

This article introduces a robust and affordable method to compute nullspace and generalized inverse of finite element operators involved in dual domain decomposition methods. The methodology relies on the operator partial factorization and on the analysis of a well chosen Schur complement. The sparse linear operator is interpreted as a network and graph centrality measures are used to select the condensation variables. Eigenvector, Katz and Page Rank centralities are evaluated. An extension to deal with symmetric indefinite systems arising from mixed finite elements is also presented. The approach is assessed on highly heterogeneous problems and one industrial application is presented: the numerical homogenization of solid propellant.

KEYWORDS

finite element tearing and interconnecting, fixing-node, floating subdomain, generalized inverse, graph centralities, nullspace detection

1 | INTRODUCTION

Domain decomposition methods such as the Finite Element Tearing and Interconnecting (FETI)¹ and its variants Total FETI (TFETI),^{2,3} Hybrid Total FETI (HTFETI),^{4,5} Adaptive Multipreconditioned FETI (AMPFETI),⁶⁻⁸ involve the resolution of semidefinite systems of equations. These systems arise when the domain decomposition has subdomains whose are not subjected to sufficient Dirichlet boundary conditions to prevent the existence of rigid body motions. It happens frequently when the number of subdomains is high and/or when the decomposition is automatically generated using a graph partitioning library. These subdomains are commonly denoted as “floating subdomains” (or substructures).⁹ The presence of floating substructures also occurs when studying free-free flexibility matrices for structural analysis.¹⁰

Finite element tearing and interconnecting (FETI) like methods are able to tackle really large-size problems while exhibiting good scalability.^{5,11} The range of application of these methods also covers for example, biomechanics,¹² structural dynamics,¹³ contact mechanics,¹⁴ digital image correlation,¹⁵ nonlinear problems with specific algorithms^{16,17} and isogeometric analysis.^{18,19}

Continuous effort has been made to be able to deal with real engineering applications that exhibit pathological components that hinder the convergence of the underlying Krylov solver, such as jagged interfaces, bad aspect ratios, strong heterogeneity, incompressibility, and so forth.^{20,21} These pathological components lead to highly ill-conditioned linear systems, making essential the use of enhanced iterative solvers. Two kinds of strategies have been proposed to increase the

This is an open access article under the terms of the [Creative Commons Attribution-NonCommercial-NoDerivs](https://creativecommons.org/licenses/by-nc-nd/4.0/) License, which permits use and distribution in any medium, provided the original work is properly cited, the use is non-commercial and no modifications or adaptations are made.

© 2022 The Author. *International Journal of Numerical Methods in Engineering* published by John Wiley & Sons Ltd.

robustness of domain decomposition solvers. The first strategy relies on augmenting the Krylov solver with a well-chosen supplementary coarse space. This supplementary coarse space (also called adaptive coarse space) is usually derived from solving local generalized eigenvalue problems.²²⁻²⁴ Since these eigenvalue computations are expensive, machine learning techniques have been proposed to reduce their number.^{25,26} The parallel load balancing also has been improved.²⁷ The second strategy is to use a block Krylov solver²⁸ or a multipreconditioned Krylov solver.^{6,28-31}

The improvement of the iterative interface solver is often pointed out when dealing with ill-conditioned problems. However, it is not the only component of the method put on severe test. The treatment of floating substructures through the automatic detection of local operator nullspaces and the computation of generalized inverses, are crucial points of the FETI methods. A misdetection of these kernels leads inevitably to the divergence of the iterative solver and ill-conditioned generalized inverses may slow down its convergence. Since the seminal work of Farhat and G eradin,⁹ few authors have investigated the problem. A treatment of substructures with internal mechanisms was proposed by Papadrakakis et al.³² More recently, generalized inverse computation and regularization techniques have been proposed in the case of known nullspace.³³ The use of incomplete factorization, the concept of fixing-nodes and a selection process based on the Perron vector have been introduced by Brzobohat y et al.³⁴ The impact of the generalized inverse computation on the convergence of the iterative solver has been investigated by the same team.^{35,36} However, these research articles do not address the case of ill conditioned local operators and most of the examples remain academic.

From our experience in the development of AMPFETI and from the simulation of ill-conditioned industrial applications, such as the numerical homogenization of woven composite⁶ and solid propellant,⁸ a robust process to detect local operators nullspaces and to compute generalized inverse turns out to be essential. The aim of this paper is to present an extension of the approach proposed by Brzobohat y et al.³⁴ in order to deal with ill conditioned operators. We typically tackle the problem of material heterogeneity and highly variable finite element mesh size. To this end, we propose several strategies to improve the selection of fixing-nodes. Most of them are based on the notion of graph centrality. Also, we provide a simple process to handle symmetric indefinite system arising from mixed finite element method for instance.

We would like to point out that the problem is really specific to the FETI like methods. For its primal counterpart, the Balancing Domain Decomposition method (BDD),³⁷ the treatment of floating subdomains is less critical since it comes into play at the preconditioner level. Also, the Dual Primal FETI method (FETI-DP)³⁸ and the Balancing Domain Decomposition by Constraints method (BDDC)³⁹ are free from this flaw since corner nodes are chosen to remove local operators nullspace.

The article is organized as follows: Section 2 recalls basic notions about generalized inverse and graph theory, Section 3 provides a short review on existing methods, while the overall methodology is introduced in Section 4. Section 5 details all the fixing-nodes selection strategies. Three numerical examples are provided in Section 6, an academic Laplace problem, an academic elastic truncated pyramid and an elastic simplified laminated composite. The first example is illustrative in order to understand how the centrality measures behave. The second example is a reproduction of the benchmark proposed by Brzobohat y et al.,³⁴ it assesses the good performance of the proposed methods. The latter example is a large ill-conditioned problem, it highlights the performance of the proposed approach and provides a comparison with the Multifrontal Massively Parallel sparse direct Solver (MUMPS) automatic defect detection. The approach is assessed on the highly ill-conditioned problem of the numerical homogenization of solid propellant in Section 7. This application also shows the performance of the specific treatment of symmetric indefinite systems proposed in Section 5.3. Finally, Section 8 concludes the paper and draws some prospects.

2 | NOTATIONS AND PRELIMINARIES

2.1 | Generalized inverse

Let $\mathcal{A} \in \mathbb{R}^{n \times n}$ be a real square, possibly singular, matrix. The (i, j) component of the matrix \mathcal{A} is denoted by \mathcal{A}_{ij} . In the following, $\mathbf{I}_n \in \mathbb{R}^{n \times n}$ is the identity matrix and $\mathbf{0}_n \in \mathbb{R}^{n \times n}$ the zero matrix. If $\alpha \subseteq \{1, \dots, n\}$ and $\beta \subseteq \{1, \dots, n\}$ are two nonempty subsets of $\{1, \dots, n\}$, we denote by $\mathcal{A}_{\alpha\beta}$ the submatrix of \mathcal{A} with components $(\mathcal{A}_{ij})_{i \in \alpha, j \in \beta}$. For convenience, if $\alpha \subseteq \{1, \dots, n\}$ is a nonempty subset, we denote by $\bar{\alpha}$ its complement: $\bar{\alpha} = \{1, \dots, n\} \setminus \alpha$. For any nonempty α and after some permutations of rows and columns, the matrix \mathcal{A} can be written by block as:

$$\mathcal{A}^* = \mathbf{P}^\top \mathcal{A} \mathbf{P} = \begin{bmatrix} \mathcal{A}_{\alpha\alpha} & \mathcal{A}_{\alpha\bar{\alpha}} \\ \mathcal{A}_{\bar{\alpha}\alpha} & \mathcal{A}_{\bar{\alpha}\bar{\alpha}} \end{bmatrix} \quad (1)$$

where \mathbf{P} is a permutation matrix. In the following, we directly consider the form (1) and we omit the permutation matrices and the star exponent.

We are interested in finding a solution of the consistent linear system $\mathcal{A}x = b$ where $\mathcal{A} \in \mathbb{R}^{n \times n}$ is singular. The defect of the matrix \mathcal{A} is denoted by k and its rank by $r = n - k$. The system is consistent if $b \in \text{Im}(\mathcal{A})$. A well known method to find a solution is to use the Moore-Penrose generalized inverse \mathcal{A}^\dagger which is the unique matrix satisfying the four Moore-Penrose conditions (see Section 5.5.2 in Reference 40).

$$\mathcal{A}\mathcal{A}^\dagger\mathcal{A} = \mathcal{A} \quad (2)$$

$$\mathcal{A}^\dagger\mathcal{A}\mathcal{A}^\dagger = \mathcal{A}^\dagger \quad (3)$$

$$\mathcal{A}\mathcal{A}^\dagger = (\mathcal{A}\mathcal{A}^\dagger)^\top \quad (4)$$

$$\mathcal{A}^\dagger\mathcal{A} = (\mathcal{A}^\dagger\mathcal{A})^\top \quad (5)$$

The Moore-Penrose generalized inverse can be computed through a singular value decomposition (SVD), $\mathcal{A} = \mathbf{U}\mathbf{\Sigma}\mathbf{V}^\top$ where $\mathbf{U} \in \mathbb{R}^{n \times n}$ and $\mathbf{V} \in \mathbb{R}^{n \times n}$ are orthogonal matrices, the diagonal matrix $\mathbf{\Sigma} \in \mathbb{R}^{n \times n}$ contains the ordered singular values of \mathcal{A} .

$$\mathbf{\Sigma} = \text{diag}(\sigma_1, \dots, \sigma_n) \quad \text{with} \quad \sigma_1 \geq \sigma_2 \dots \geq \sigma_r > \sigma_{r+1} = \dots = \sigma_n = 0$$

The Moore-Penrose generalized inverse is given by $\mathcal{A}^\dagger = \mathbf{V}\mathbf{\Sigma}^\dagger\mathbf{U}^\top$ where $\mathbf{\Sigma}^\dagger = \text{diag}(\sigma_1^{-1}, \dots, \sigma_r^{-1}, 0, \dots, 0)$. The Moore-Penrose generalized inverse is often considered as the “best generalized inverse” since it minimizes the Frobenius norm $\|\mathcal{A}\mathcal{A}^\dagger - \mathbf{I}_n\|_F$. It is however very expensive to evaluate, common algorithms have complexities in $O(n^3)$. The storage cost is also high because \mathbf{U} and \mathbf{V} are dense matrices. The nullspace of \mathcal{A} is also provided by the singular value decomposition, it is the k last columns of the matrix \mathbf{V} . Considering the treatment of floating subdomains in dual domain decomposition methods, any matrix satisfying (2) is suitable and it is not necessary to fulfill all the Moore-Penrose conditions. We will denote by \mathcal{A}^\dagger a generalized inverse satisfying (2). This work proposes a robust but cheap methodology to compute such a matrix.

2.2 | Reminder on graphs

The present work makes use of tools coming from Graph (also called network) theory, useful notions are given hereafter. The reader interested in a wider documentation can refer to the book.⁴¹

2.2.1 | Undirected graph

A graph \mathcal{G} is defined by two sets (V, E) . The first set V is a collection of vertices while the second set E contains edges. An edge is a pair of vertices $(u, v) \in V \times V$ that represents some kind of link between u and v . If this link does not depend on the ordering, the graph is said undirected. In this work, we only consider undirected simple graphs, for example, graphs without any self-edge (i.e., a pair (u, u) , $u \in V$) nor multi-edge (a graph contains a multi-edge if there are two or more edges connecting the same vertices). From now on, we denote by n_v the number of vertices and by n_e the number of edges.

2.2.2 | Weighted graph

It will be useful to characterize the strength of an edge $(u, v) \in E$ by a strictly positive scalar $\omega_{uv} > 0$. A weighted graph is thus defined by a graph and a set of weights. Note that an unweighted graph can be represented with a weighted graph with an uniform weight set to 1.

2.2.3 | The adjacency matrix

The adjacency matrix of the graph is the matrix $\mathbf{A} \in \mathbb{R}^{n_v \times n_v}$ with elements a_{uv} such that

$$a_{uv} = \begin{cases} \omega_{uv} > 0 & \text{if there is an edge between vertices } u \text{ and } v \\ 0 & \text{otherwise.} \end{cases}$$

In this work, we only consider undirected simple graphs so \mathbf{A} remains symmetric and $a_{uu} = 0 \forall u \in V$ since self-edges are not allowed.

2.2.4 | Degree of a vertex

The degree of a vertex u is the scalar $d_u = \sum_{v=0}^{n_v} a_{uv}$. Let \mathbf{D} be the diagonal matrix of order n_v such that $\mathbf{D} = \text{diag}(d_1, \dots, d_{n_v})$. For an undirected unweighted graph, the degree d_u is simply the number of edges connected to u .

2.2.5 | The graph Laplacian

The graph Laplacian is alternative representation of undirected weighted graph. The matrix form of the graph Laplacian is the symmetric matrix $\mathbf{L} \in \mathbb{R}^{n_v \times n_v}$ defined by $\mathbf{L} = \mathbf{D} - \mathbf{A}$. The graph Laplacian has various applications such as graph partitioning or network visualization (see e.g., [Reference 41, Section 6.14]).

2.2.6 | Graph centrality

One of the frequent applications of graph theory tools is to find out which vertex is the most important in a network. This importance can be described in several ways, which translate into different measures of graph centrality. These measures usually depend on the graph topology and on the strength of the graph edges. It will be defined by a score vector $\mathbf{c} \in \mathbb{R}_+^{n_v}$. The graph centralities used in this work will be presented in Section 5.2.

3 | BRIEF REVIEW OF EXISTING APPROACHES

3.1 | The pioneering work of Farhat and G eradin

Farhat and G eradin⁹ were one of the first to investigate the treatment of floating subdomains in structural mechanics. They proposed three strategies to cheaply compute the generalized inverse and the nullspace of the stiffness matrices.

The first one relies on the null pivots detection of the Crout factorization (also called LDLT factorization) with symmetric pivoting. Indeed, if $\mathcal{A}_{\alpha\alpha}$ is invertible and the k last pivots are null pivots both,

$$\begin{bmatrix} \mathcal{A}_{\alpha\alpha}^{-1} & \mathbf{0} \\ \mathbf{0} & \mathbf{0} \end{bmatrix} \quad \text{and} \quad \begin{bmatrix} \mathcal{A}_{\alpha\alpha}^{-1} & -\mathcal{A}_{\alpha\alpha}^{-1} \mathcal{A}_{\alpha\bar{\alpha}} \\ \mathbf{0} & \mathbf{I}_k \end{bmatrix} \quad (6)$$

fulfill the first Moore-Penrose condition (2) and a basis of the nullspace is given by the $n \times k$ matrix \mathbf{R} .

$$\mathbf{R} = \begin{bmatrix} -\mathcal{A}_{\alpha\alpha}^{-1} \mathcal{A}_{\alpha\bar{\alpha}} \\ \mathbf{I}_k \end{bmatrix} \quad (7)$$

The permutation ensuring that $\mathcal{A}_{\alpha\alpha}$ is nonsingular is generated by the pivoting process. The defect computation relies on the distinction between null and small pivots which requires a user-defined small constant ϵ . This parameter may be hard to setup in presence of ill conditioned systems. A ‘‘modern’’ version of this approach is to let up-to-date direct solvers, such as MUMPS⁴² or Dissection,⁴³ detect null pivots and compute the generalized inverse and nullspace. As will be shown in Section 6.4, even the most advanced solvers such as MUMPS can be put in severe test with specific pathological tests.

The second method proposed in the article⁹ needs to know *a priori* an upper bound of the defect q and a renumbering of the unknowns ensuring that null pivots arise at the end of the factorization. For mechanical problems such a renumbering can be defined by numbering last all translational unknowns attached to three non aligned nodes. A Crout factorization without pivoting is performed up to the step $n - q + 1$, then a SVD is applied on the remaining Schur complement to obtain the true defect k . The rest of the factorization is done with full pivoting and last k pivots are considered as null

pivots. This method still relies on an user defined constant but the SVD is applied on a small Schur complement with a better condition number.

The third method, initially thought for structural mechanics, needs to know the nullspace in the case of a totally unrestrained subdomain, that is, a subdomain without any Dirichlet boundary condition. Let \mathbf{R}_u be a basis of this totally unrestrained nullspace. In the context of 3D elastostatics, if the subdomain is connected, without mechanism and totally unrestrained, this nullspace is known. It is composed of the six rigid body modes (3 translations and 3 rotations). These rigid body modes can be built explicitly using a geometric procedure. For an unrestrained subdomain, the generalized inverse can be computed using (6) and considering the six last pivots as null pivots. For partially restrained subdomains the strategy is slightly more complex. Let n_D be the number of unknowns subjected to Dirichlet boundary conditions. A boolean matrix \mathbf{E} of size $n \times n_D$ is introduced with $E_{ij} = 1$ if the unknown j is constrained by the i -th boundary condition and $E_{ij} = 0$ elsewhere. A SVD is then performed on the matrix $\mathbf{Z} = \mathbf{E}^T \mathbf{R}_u$ to compute the actual defect of the operator \mathcal{A} . The actual nullspace which is a linear combination of the columns of \mathbf{R}_u can also be retrieved from the singular value decomposition. Once the defect k is known, the generalized inverse can also be computed considering the last k pivots as null pivots. From a mechanical point of view, the matrix \mathbf{Z} looks like the virtual work produced by the Dirichlet boundary conditions when considering rigid body motions as virtual displacements. Again, the defect computation involves a small constant for the SVD of the matrix \mathbf{Z} . The defect computation is less sensitive to the condition number of the stiffness matrix since both \mathbf{E} and \mathbf{R}_u are kinematic quantities. Indeed, \mathbf{E} and \mathbf{R}_u depend on the Dirichlet boundary conditions and on the geometry of the mesh but not on the material law used. This property may be useful when dealing with highly heterogeneous subdomains. Only the condition number of the generalized inverse will be impacted. The condition number of \mathbf{R}_u depends however on the slenderness of the subdomain. Scaling procedures have been proposed to improve this point.³² This algebraic–geometric method requires the absence of internal mechanism. Their detection and removal have been investigated with the mechanism buster algorithm⁹ and this constraint has been overcome few years later with geometric procedures.³² This method is however hard to generalize to meshes composed of exotic element types such as, cohesive zone elements⁴⁴ or pressure-displacement mixed elements⁴⁵ or multipoint constraints (MPC).

3.2 | The incomplete factorization and fixing-nodes framework

The previous methods are focused on the defect computation, they do not investigate the condition number of the resulting generalized inverse. A continuous progress has been made in this field by the research group of Z. Dostál^{33,34,36,46,47} which led to the incomplete factorization framework and the concept of fixing-nodes.

As pointed out in Brzobohatý et al.,³⁴ all previous methods can be reformulated in the incomplete factorization framework. Only symmetric semi-definite matrices were considered in this article and the framework was expressed in terms of incomplete Cholesky factorization. If the symmetry provides useful properties such as the Haynsworth inertia additivity formula, it is not a limitation of the approach. In the following, we use the incomplete \mathbf{LU} factorization. In the case of a symmetric semi-definite matrix, one simply has to replace all matrices \mathbf{U} by \mathbf{L}^T .

If c is a non empty subset of $\{1, \dots, n\}$, the incomplete \mathbf{LU} factorization is

$$\mathcal{A} = \begin{bmatrix} \mathcal{A}_{\bar{c}\bar{c}} & \mathcal{A}_{\bar{c}c} \\ \mathcal{A}_{c\bar{c}} & \mathcal{A}_{cc} \end{bmatrix} = \begin{bmatrix} \mathbf{L}_{\bar{c}\bar{c}} & \mathbf{0} \\ \mathbf{L}_{c\bar{c}} & \mathbf{I} \end{bmatrix} \begin{bmatrix} \mathbf{U}_{\bar{c}\bar{c}} & \mathbf{U}_{\bar{c}c} \\ \mathbf{0} & \mathbf{S}_{cc} \end{bmatrix}. \quad (8)$$

As long as $\mathcal{A}_{\bar{c}\bar{c}}$ remains full rank, a generalized inverse of \mathcal{A} is given by

$$\mathcal{A}^+ = \begin{bmatrix} \mathbf{U}_{\bar{c}\bar{c}}^{-1} & -\mathbf{U}_{\bar{c}\bar{c}}^{-1} \mathbf{U}_{\bar{c}c} \mathbf{S}_{cc}^\dagger \\ \mathbf{0} & \mathbf{S}_{cc}^\dagger \end{bmatrix} \begin{bmatrix} \mathbf{L}_{\bar{c}\bar{c}}^{-1} & \mathbf{0} \\ -\mathbf{L}_{c\bar{c}} \mathbf{L}_{\bar{c}\bar{c}}^{-1} & \mathbf{I} \end{bmatrix}. \quad (9)$$

Since the Schur complement \mathbf{S}_{cc} is a small dense matrix, the use of the Moore–Penrose generalized inverse is reliable and affordable here. The matrix $\mathcal{A}_{\bar{c}\bar{c}}$ being full rank, the Schur complement is rank deficient due to the property

$$\det(\mathcal{A}) = \det(\mathbf{S}_{cc}) \cdot \det(\mathcal{A}_{\bar{c}\bar{c}})$$

For well conditioned test cases, the use of a “large enough” set c , for which $\text{card}(c) > k$, suffices. For ill conditioned systems however, to choose good *candidates* for the incomplete factorization remains essential, in order to get $\mathcal{A}_{\bar{c}\bar{c}}$ and

\mathcal{A}^+ reasonably well conditioned, and to facilitate determination of the defect of \mathbf{S}_{cc} . In Brzobohatý et al.,³⁴ nodes of the mesh corresponding to the unknowns of the set c are called fixing-nodes. Since these fixing-nodes define the unknowns used for the static condensation, the attributes “fixing” and “condensation” are used interchangeably in the following. Also, for symmetric indefinite systems, we will use the term fixing-variables since all variables of fixing-nodes will not be put in the set c .

From a mechanical point of view, these fixing-nodes must not be aligned, and well distributed within the substructure. From these considerations, a two-step construction process has been proposed.³⁴ First, the subdomain mesh is virtually split into $M \geq k$ parts (also called color in the following). Then a fixing-node close to the center of each color is selected using an heuristic.

4 | OVERALL METHODOLOGY

This section introduces the overall methodology to detect the nullspace and to compute the generalized inverse. It follows the two-step construction process proposed in Brzobohatý et al.³⁴ As before, the subdomain mesh is virtually split into $M \geq k$ parts, then one fixing-node is selected in each part. Note that, if the initial subdomain is not connected, the number of parts must be adapted. Since an upper bound of the defect is usually known for a connected subdomain, the overall methodology is logically applied to each connected component of the subdomain. The main purpose of this work is to define new selection strategies of fixing-node in order to tackle highly ill-conditioned systems. The methodology is summed up in Algorithm 1 and illustrated with Figure 1.

4.1 | Selection process of fixing-nodes

In this work, several selection strategies are proposed and compared, they will be detailed in Section 5. We only give the common framework here. The selection strategies can be expressed as a vector-valued function f of some graph \mathcal{G} such as $f(\mathcal{G}) = \mathbf{s} \in \mathbb{R}_+^p$ where p is the number of nodes of the considered color. All the components of \mathbf{s} are positive, they give the score of the corresponding node. The node with the highest score is selected as the fixing-node. The application of this selection process to each color provides a set of fixing-nodes, all unknowns linked to these nodes are put in the set of fixing-variables c . Once the set of fixing-variables is defined, the incomplete factorization is performed (8).

Algorithm 1. Fixing-nodes selection algorithm

Verify that the initial mesh is connected (if not apply Algorithm 1 to each connected component).

Virtually split the mesh in M connected parts

for each part **do**

 Apply selection strategy (see Section 5)

end for

Filter duplicated nodes if needed

Filter mixed variables if needed (see Section 5.3)

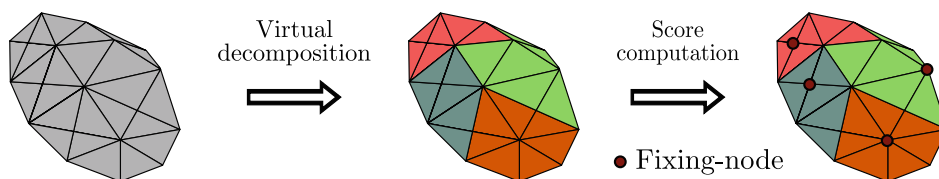


FIGURE 1 Schematic representation of the overall methodology

4.2 | Nullspace computation and generalized inverse of the Schur complement

The incomplete factorization framework leads to a small dense Schur complement \mathbf{S}_{cc} of order m . The matrix \mathbf{A}_{cc} being full rank, the Schur complement is rank deficient. The use of the Moore-Penrose generalized inverse is affordable and applied here. As explained before, it is computed through a singular value decomposition. The singular value decomposition also provides the nullspace of the Schur complement \mathbf{R}_c . The nullspace of the full matrix is deduced from \mathbf{R}_c

$$\mathbf{R} = \begin{bmatrix} -\mathbf{A}_{cc}^{-1} \mathbf{A}_{cc} \mathbf{R}_c \\ \mathbf{R}_c \end{bmatrix} \quad (10)$$

The estimation of the rank of \mathbf{S}_{cc} involves a user defined threshold ϵ to distinguish between null singular values and small ones. Two criterion are classically used. The first one compares the current singular value with respect to the largest one

$$\text{Relative criterion: } \sigma_j \leq \epsilon \sigma_1 \quad (11)$$

Another possibility is to look for the jump between two adjacent singular values

$$\text{Jump criterion: } \sigma_{j+1} \leq \epsilon \sigma_j \quad (12)$$

The validity range of the threshold ϵ is, by definition, the range $[\epsilon_{min}, \epsilon_{max}]$ that leads to a correct evaluation of the defect. If the selection strategy is well chosen, both criteria behave similarly most of the time and the validity range of the threshold covers several decades. The jump criterion may have the advantage when several jumps of material coefficients are present in the underlying physical problem.

More complex strategies may be proposed, based on unsupervised learning for example. Indeed, the problem can be reformulated as a clustering problem where the singular values of the Schur complement are the sample data. The clustering problem intends to split singular values into two clusters corresponding to null and not null singular values. Several models of the machine learning scikit-learn library (<https://scikit-learn.org/>) have been tried in this work such as Gaussian mixture model and K-means. However, these advanced techniques have been used as is, without specific tuning of their parameters.

We were not able to build a clustering process outperforming the classical criteria especially for indeterminate cases such as symmetric indefinite systems (see Section 7.3). The sample data are probably too scarce. In the context of domain decomposition methods, an interesting possibility would be to share the singular values of all local stiffness operators to increase the number of data. Supervised learning or semi-supervised learning could be employed to replace the relative and the jump criterion. It seems a bit excessive here because one deals with one dimensional data. The use of (semi-)supervised learning could be much more helpful for the fixing-nodes selection, as an alternative to the proposed methodology. Here, the work of Heinlein et al.²⁵ might be a source of inspiration.

4.3 | Some practical remarks

4.3.1 | About the number of fixing-nodes

An important parameter of the method is the number of condensation nodes. This number must be large enough to remove the non-trivial nullspace of the operator. For example, three non-aligned nodes per connected component without too much heterogeneity suffice for a 3D mechanical problem. In the implementation, an automatic rule-of-thumb is proposed. Let M_{min} be the minimum number of nodes needed to remove the non trivial nullspace of a connected totally floating subdomain. For each connected component, the automatic rule-of-thumb is $M = (M_{min} + 1)$ if $M_{min} > 1$, $M = M_{min}$ otherwise. For very heterogeneous problems and depending on the type of centrality used, two colors may select the same node. This node being at the interface between these two colors. This problem can be solved simply by slightly increasing the number of condensation nodes. Another strategy is to process the colors successively. If a color proposes an already selected node, this node is refused and the second best node is picked up. For 3D mechanical problems, four condensation nodes per connected component are enough most of the time.

4.3.2 | About the impact on the convergence of the FETI iterative solver

The impact on the FETI domain decomposition method is pretty clear when the nullspace of local operators are wrongly evaluated. In this case, the FETI projector is wrong and the FETI system is not equivalent to the original system anymore. The iterative solver very often diverges and/or leads to a wrong solution. If the nullspace is correctly evaluated but the generalized inverse does not fulfil (2) reasonably well, Kučera et al.³⁵ have shown that the convergence of the FETI method is slightly degraded. The negative impact on the convergence is limited thanks to the stabilization effect of the FETI projector. This is typically the case for the Total FETI variant where the nullspace is known *a priori*. Though the improvement of the condition number is always worthwhile, the main advantage of proposed method is to always lead to a wide threshold validity range.

4.3.3 | About the implementation

The virtual split is performed using an automatic graph partitioner such as METIS or Scotch. The condensation node selection method is easily implemented in parallel. Each color is processed independently with shared memory parallelism. For graph centralities that require solving linear systems, iterative solvers with low memory cost are used. The incomplete factorization is performed using the functionality of the MUMPS solver that internally handles the numbering of the unknowns to limit the fill-in of the factorization. It relies on the SCOTCH or METIS library in our case.

5 | ON THE CHOICE OF FIXING-NODES

In this section, we present different strategies for choosing the fixing-nodes. Most of them take advantage of graph theory and in particular of the notion of centrality. Proposed strategies have to bear in mind various objectives:

- to lead to good fixing-nodes candidates, which means to minimize the condition number of the operators, and to give a clear distinction between null and small singular values,
- to present a low computational cost,
- to be robust (meaning that the determination hardly ever fail).

For ill-conditioned system such as highly heterogeneous problems, to pick up a fixing-node close to the center of each color is not sufficient and new strategies are needed. To illustrate this statement let us consider an elastostatic structure made of rubber and steel. From a mechanical viewpoint, adding Dirichlet boundary conditions on the fixing-nodes should stiffen this structure. Besides being well distributed, fixing-nodes should clearly be in the steel part. Selection strategies will mimic this rule-of-thumb to propose centrality measures with well chosen edge weights. From an algebraic viewpoint, fixing-variables c should correspond to large diagonal terms in the matrix in order to improve the condition number of \mathcal{A}_{cc}^- and \mathcal{A}^+ and to facilitate the estimation of the defect of the matrix.

5.1 | Modelling of finite element operators as graphs

Graph centrality measures are useful tools to characterize the most important vertices of a graph. The meaning of the word "importance" obviously depends on the network under consideration and the application. Once the graph is chosen, the key point is to build vertex and edge weights and to choose a centrality measure such that the more central the vertex is, the more involved in the cohesiveness of the network. Thus, this process involves a two-step modelling. The first one defines connection between vertices and maps the finite element operator to the graph (described here by the adjacency matrix). The second step defines how vertices and edges contribute to the cohesiveness of the network.

$$\begin{array}{ccccc} \mathbb{R}^{n \times n} & \xrightarrow{\text{Network model}} & \mathbb{R}^{n_v \times n_v} & \xrightarrow{\text{Centrality model}} & \mathbb{R}_+^{n_v} \\ \mathcal{A} & \mapsto & \mathbf{A} & \mapsto & \mathbf{s} \end{array}$$

5.1.1 | Taking into account the operator

Different graphs naturally arise in the context of finite element problems. The finite element mesh, via its connectivity table, defines a first graph where the vertices are the nodes of the mesh and two nodes are linked by an edge if they belong to the same element. Also, the finite element operator can be considered as a graph where the vertices are the degrees of freedom. An edge links two degrees of freedom if there is an associated non-zero extra-diagonal term. For problems involving more than one degree of freedom per node, the graph associated with the operator can be much larger than the one built on the mesh. In the present work, we choosed to use the “nodal” graph because of its smaller size. This “nodal” graph can be seen as finite element nodes interconnected by springs. We note however that for very anisotropic problems, the latter option may be more suited.

5.1.2 | Edge weights approximation

The finite element operator provides a natural way to define the strength of an edge. Indeed, the strength of the link between two vertices can be defined by the amplitude of the extra-diagonal term. This vision has been exploited successfully by algebraic multigrid methods where depending on the value of the extra-diagonal term, one unknown strongly depends (or strongly influences) another (see for instance Chap. 8 in the book⁴⁸ and the references herein).

The main difference here is that the vertices of the graph are the node of the mesh. So except for the case of the Poisson problem, there is not a direct mapping between nodes and degrees of freedom. Several edge weights may be proposed:

- **Full weight:** Let δ_u (resp. δ_v) be the set of degrees of freedom associated with the node u (resp. v). For two linked nodes u and v , the full weight of the edge (u, v) is defined as the sum of all extra diagonal terms

$$\omega_{uv} = \sum_{i \in \delta_u} \sum_{j \in \delta_v} |\mathcal{A}_{ij}|$$

- **Lumped weight:** Degrees of freedom are associated with physical quantities (temperature, displacement, etc.). Let ϕ^i be the physical quantity associated with the unknown i . The lumped weight of the edge is defined as the sum of all extra diagonal terms corresponding to the same physical quantity.

$$\omega_{uv} = \sum_{\{i \in \delta_u, j \in \delta_v \mid \phi^i = \phi^j\}} |\mathcal{A}_{ij}|$$

- **Uniform weight:** all edges have a weight equal to 1.

The finite element operator is a sparse matrix that is stored most of the time in the Compressed Sparse Column Format (CSC) or Compressed Sparse Row Format (CSR). Looking up for a specific term in \mathcal{A} involves a binary search which is costly. Also, the lumped and full edge weight leads to the same centrality measure for isotropic problems. For this reason, the full weight version is not considered in the following.

5.2 | Available selection methodologies

All the methods presented here take the form of computing a positive score s (also called centrality) for each node of a graph and selecting the node with highest score.

5.2.1 | Random selection

Attributing randomly a score to each node is the simplest possible strategy. This approach was proposed for the HTFETI method.⁴⁹ For a homogeneous problem with a ruled mesh, it has been shown that the probability of a “bad choice” decreases strongly with the number of fixing-nodes. Here a “bad choice” corresponds to the choice of aligned nodes.

It seems difficult to improve this approach to deal with ill conditioned cases, apart from increasing the number of fixing-nodes.

5.2.2 | Gravity center

Bearing in mind that the fixing-nodes must be evenly distributed over the subdomain, one possible approach is to select the closest node to the center of gravity of each subpart. Let $\mathbf{m}_i \in \mathbb{R}^3$ be the position vector of the node i . An approximation of this gravity center may be:

$$\mathbf{m}_g = \frac{\sum_{j=1}^{n_v} \varpi_j \mathbf{m}_j}{\sum_{j=1}^{n_v} \varpi_j} \quad (13)$$

where ϖ_j is a weight associated with the node j . For node i , the score is defined as

$$s_i = \frac{1}{\ell + \|\mathbf{m}_i - \mathbf{m}_g\|_2} \quad (14)$$

where ℓ is the unit length. So the closer node i is to the center of gravity, the higher the score is. This geometric approach is simple but choosing appropriate weights is an inextricable task. Assigning an equal weight to all the nodes of the mesh may lead to selecting one close to very refined area. For homogeneous problems, this is typically a bad choice since it does not correspond to large diagonal terms of the stiffness matrix (see Figure 2). Indeed, the diagonal terms of the stiffness matrix is proportional to the Jacobian of the connected elements.

A weight proportional to the diagonal terms of the stiffness matrix may seems a better choice but it is easy to find simple examples where this strategy fails (see e.g., Figure 3).

5.2.3 | Eigenvector centrality

Let $\{\lambda_i, \mathbf{q}_i\}_{1 \leq i \leq n_v}$ be the eigenmodes of the adjacency matrix \mathbf{A} with $\lambda_1 \geq \lambda_2 \dots \geq \lambda_{n_v}$. The eigenvector centrality is simply defined by the components of the dominant eigenvector $\mathbf{s} = \mathbf{q}_1$ (also known as the Perron vector). Thanks to the Perron–Frobenius theorem all the components of this vector are of the same sign (assumed to be positive here). With this measure, the centrality of a node i is proportional to the sum of the centralities of its neighbors. Thus a node can achieve a high centrality score either by having a lot of neighbors with average centrality, or by having a few neighbors with high centrality. Since \mathbf{A} is symmetric, the evaluation of this centrality measure is really inexpensive and few steps of the Lanczos method leads to a good approximation. The use of the eigenvector centrality has already been proposed by Brzobohatý et al.,³⁴ the adjacency matrix considered was associated with the unweighted graph. In this work, the eigenvector centrality is computed on the weighted graph which allows to take into account material heterogeneity for instance.

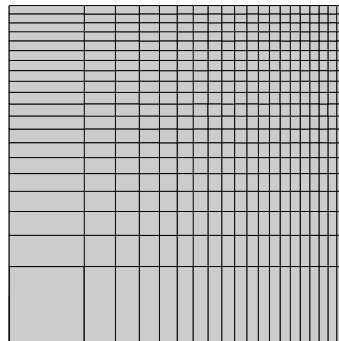


FIGURE 2 Small counter example: Homogeneous material with variable mesh size. A uniform weight will select a node in the upper right part of the square

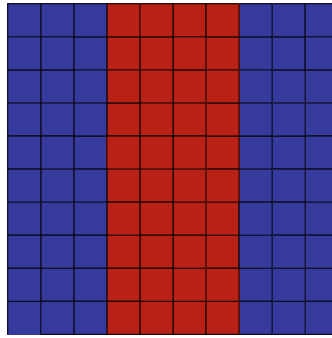


FIGURE 3 Small counter example: Heterogeneous material where the red part is much softer than the blue ones. Whatever the weight, a gravity center based method will always select the central node because of the symmetry of the problem

5.2.4 | Katz centrality

The eigenvector centrality is only influenced by the edges of the graph. In our application, it turns out to be useful to add an intrinsic contribution to the centrality of each node. Since, from a mechanical point of view, nodes associated with stiff elements are obviously good fixing-node candidates, we would like to assign a specific importance to each node based on the diagonal terms of the stiffness matrix. The Katz centrality⁵⁰ (see also Section 7.1.3 in the book⁴¹) allows such a behavior, it is the solution of the system

$$(\mathbf{I} - \alpha^* \mathbf{A})\mathbf{s} = \boldsymbol{\beta} \quad (15)$$

where α^* is a scalar parameter and $\boldsymbol{\beta} \in \mathbb{R}^{n_v}$ is the intrinsic part of the centrality. To ensure that $(\mathbf{I} - \alpha^* \mathbf{A})$ is invertible, the parameter α^* has to be in the interval $[0, \lambda_1^{-1}[$, where λ_1 is the largest eigenvalue of \mathbf{A} . It is convenient to express this parameter with respect to λ_1 to get a robust process, the new parameter is $\alpha \in [0, 1[$, such that $\alpha^* = \alpha \lambda_1^{-1}$.

The value of the intrinsic centrality vector $\boldsymbol{\beta}$ is a parameter of the method. It has to be consistent with the choice made for the edges weights. Thus, all nodes have the same intrinsic centrality equal to 1 if the uniform edge weight is chosen. If full or lumped edge weight are used, the intrinsic centrality of node u , β_u is defined as:

$$\beta_u = \sum_{i \in \delta_u} |\mathcal{A}_{ii}|$$

where δ_u be the set of degrees of freedom associated with the node u .

From a computational point of view, the Katz centrality remains cheap since it only requires the estimation of the largest eigenvalue of \mathbf{A} and the resolution of (15). The latter system which is symmetric positive definite, can be easily to solve with an iterative solver such as the Conjugate Gradient. The dominant eigenvector \mathbf{q}_1 is a good initial estimate.

5.2.5 | PageRank centrality

With the Katz centrality, a node shares its centrality whatever the number of its neighbors. It may be undesirable when the graph exhibits a large vertex degree variation. The PageRank centrality has been proposed to attenuate this phenomenon.⁵¹ Here, the centrality shared by a node to its neighbors is divided by its degree. Then nodes that point to many others pass only a small amount of centrality on to each of those others, even if their own centrality is high. The PageRank centrality is the solution of the system

$$(\mathbf{I} - \alpha \mathbf{A} \mathbf{D}^{-1})\mathbf{s} = \boldsymbol{\beta} \quad (16)$$

where, as in the Katz centrality, $\alpha \in [0, 1[$, $\boldsymbol{\beta} \in \mathbb{R}^{n_v}$ is the intrinsic part of the centrality. The matrix \mathbf{D} is the diagonal matrix of nodal degree (see Section 2). By construction, the graph is free of any isolated vertex so all diagonal terms are strictly positive. The intrinsic centrality vector $\boldsymbol{\beta}$ is defined as in Section 5.2.4. In contrast with the Katz centrality, the computation of the largest eigenvalue of \mathbf{A} is no more needed since $(\mathbf{I} - \alpha \mathbf{A} \mathbf{D}^{-1})$ is invertible as long as $0 \leq \alpha < 1$. The

system (16) is however unsymmetric, it is solved with a Biconjugate Gradient Stabilized method (BICGSTAB). One way to recover symmetry is to use a two-step scheme, solving first $(\mathbf{D} - \alpha\mathbf{A})\mathbf{s}^* = \boldsymbol{\beta}$ then $\mathbf{s} = \mathbf{D}\mathbf{s}^*$. In practice, the non-symmetry of the system is not penalizing since the BICGSTAB solver converges in few iterations so this two-step scheme has not been used.

5.2.6 | Cross-eigenvector

Most of the previous approaches make use of the adjacency matrix. An alternative method using the Laplacian matrix has been proposed in a previous article.⁵² The score vector called Cross-eigenvector requires the computation of the eigenvectors associated with the smallest eigenvalues of the Laplacian matrix. A comparison with the eigenvector centrality for a homogeneous Laplace problem has been provided in the article,⁵² showing the good performance of the Cross-eigenvector. However, for three dimensional problems, the four smallest eigenvalues of the Laplacian matrix are needed. Computing the smallest eigenvalues is a complex and costly task especially when the system is ill conditioned. This method has not been considered further in this work.

5.3 | Treatment of symmetric indefinite systems

Symmetric indefinite systems occurs in many computational science and engineering problems. In the domain of computational mechanics, it naturally arises when studying problems involving mixed finite elements such as the Navier-Stokes equation in fluid mechanics or in the analysis of almost incompressible material with three fields mixed elements (see the book^{45,53} Sections 2.6 and 5.5). For these problems, matrices are *highly indefinite* in the sense that they have many eigenvalues of both signs. Moreover, the unknowns are linked to various physical quantities: pressure, velocity in the former case and displacement, pressure, change of volume in the latter one. If neither specific row-column scaling nor nondimensionalization are performed, matrices are usually ill conditioned. Typically, the stiffness operator obtained with three field mixed elements exhibits small negative eigenvalues. The presence of these small negative eigenvalues makes the computation of generalized inverse arduous. Indeed, without any specific treatment the Schur complement \mathbf{S}_{cc} also possesses eigenvalues of both signs. The distinction between singular values associated with small negative eigenvalues due to the mixed form and small positive eigenvalues induced by the presence of rigid body motions becomes unclear.

Here, the addition theorem for Schur complements of Hermitian matrices (see Chap. 1 in the book⁵⁴), also called Haynsworth inertia additivity formula, is an useful tool. The inertia of a Hermitian matrix \mathcal{A} (symmetric in our case) is defined as the ordered triplet

$$\text{In}(\mathcal{A}) = (p(\mathcal{A}), q(\mathcal{A}), n(\mathcal{A}))$$

whose components are respectively the numbers of positive, negative, and zero eigenvalues of \mathcal{A} . Still considering a splitting of the form (8) and assuming $\mathcal{A}_{\bar{c}\bar{c}}$ nonsingular, the addition theorem for Schur complements of Hermitian matrices states that

$$\text{In}(\mathcal{A}) = \text{In}(\mathcal{A}_{\bar{c}\bar{c}}) + \text{In}(\mathbf{S}_{cc}).$$

Thus, to avoid \mathbf{S}_{cc} having negative eigenvalues, it suffices to force them to be in the spectrum of $(\mathcal{A}_{\bar{c}\bar{c}})$. In the context of mixed finite element, after the selection of fixing-nodes, a simple way to proceed is to remove all unknowns associated with mixed variables from the set c . The benefit of this approach is exemplified in Section 7.

6 | NUMERICAL EXAMPLES

In Brzobohatý et al.,³⁴ the quality of a generalized inverse is evaluated from the violation of the Moore-Penrose conditions (2)–(5), and regarding the effective condition number of \mathcal{A}^+ and the condition number of $\mathcal{A}_{\bar{c}\bar{c}}$. The effective condition number is defined as

$$\overline{\text{cond}}(\mathcal{A}) = \frac{\lambda_1}{\lambda_r}$$

where λ_1 is the largest eigenvalue and λ_r is the smallest not null eigenvalue. The classical condition number of an invertible matrix \mathbf{M} is denoted by $\text{cond}(\mathbf{M})$. In this study, we limit our attention to these two condition numbers. Again, to compute the small eigenvalues of ill-conditioned matrices is a complex task. These condition numbers are only computed for the academic examples in Sections 6.2 and 6.3. For large scale examples, the performance of the method is analyzed with respect to the validity range of the threshold involved in the defect computation of the Schur complement \mathbf{S}_{cc} (see the definition in Section 4.2).

6.1 | Remarks on the implementation and hardware computing resources

All strategies have been implemented in the AMPFETI module of the finite element suite Z-set (<http://www.zset-software.com/>). The MUMPS solver⁴² (version 5.3.5, <http://mumps.enseeiht.fr/>) is used in association with the BLAS library provided by Intel 17.0.4 MKL, for partial factorization and associated solves (reduction and expansion phases). Eigen library (version 3.3.8, <http://eigen.tuxfamily.org/>) is used for dense linear algebra, for the singular value decomposition of the Schur complement and for all iterative solvers involved in the computation of centrality measures. The eigenvalues computation needed for the evaluation of condition numbers make use of the ARPACK library through the Python module `scipy.sparse.linalg` and the Z-set Python interface.

6.2 | Academic thermal 2D examples

This section provides small academic examples in order to understand the behavior of the various centrality measures. The problem considered is the steady-state heat equation on the unit square without any boundary Dirichlet condition $\text{div}(\kappa \text{ grad } u) = 0$ (see Figure 4).

The square is made of two different materials with thermal conductivity κ_r (resp. κ_b) for the red (resp. blue) area. Three conductivity ratio will be considered $\kappa_r/\kappa_b \in (10^{-2}, 1, 10^2)$. The unit square is discretized with a 20×20 Q1 finite elements. The conduction operator arising from the finite element discretization is singular, its nullspace is the constant vector $\mathbf{R} = \mathbf{1}_n$. It corresponds to floating subdomains when the FETI method is used to solve steady-state thermal problems. We use only one fixing-node since the defect is 1.

6.2.1 | Comparison of all methods

For Katz and PageRank centralities which depend on the parameter α , nine values are tested (0.1, 0.2, 0.3, 0.4, 0.5, 0.6, 0.7, 0.8, 0.9), only the best results, with respect to the value of α , are displayed. The best result is marked with an exponent \square^b . The influence of the parameter α is discussed in Section 6.2.2. The lumped weight is used in the section.

The results of all methods are shown in Table 1. To visualize the behavior of centrality measures, the normalized score of the Weighted Perron, Katz and PageRank centralities are plotted in Figures 5, 6 and 7.

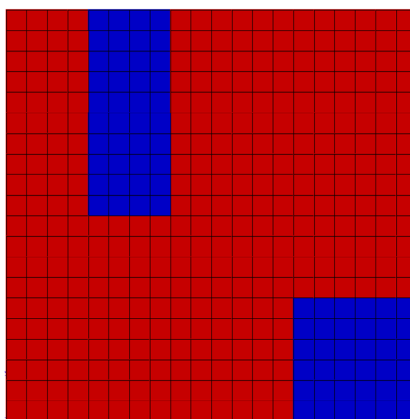


FIGURE 4 Academic thermal example, the unit square is made of two different material with conductivity κ_r and κ_b

TABLE 1 Academic thermal example: Comparison of all methods

(A) Results for $\kappa_r/\kappa_b = 10^0$		
cond(\mathcal{A})	2.04e+03	
Strategy	cond(\mathcal{A}_{cc}^-)	cond(\mathcal{A}^+)
Mumps	2.04e+03	1.76e+03
Gravity center	1.10e+03	1.10e+03
Perron	1.10e+03	1.10e+03
Katz ^b	1.10e+03	1.10e+03
PageRank ^b	2.64e+03	2.48e+03
Weighted Perron	1.10e+03	1.10e+03
Weighted Katz ^b	1.10e+03	1.11e+03
Weighted PageRank ^b	1.25e+03	1.30e+03
(B) Results for $\kappa_r/\kappa_b = 10^{-2}$		
cond(\mathcal{A})	1.82e+06	
Strategy	cond(\mathcal{A}_{cc}^-)	cond(\mathcal{A}^+)
Mumps	1.82e+06	1.56e+06
Gravity center	9.47e+05	9.56e+05
Perron	9.47e+05	9.56e+05
Katz ^b	9.47e+05	9.56e+05
PageRank ^b	6.38e+05	6.38e+05
Weighted Perron	6.37e+05	6.37e+05
Weighted Katz ^b	6.37e+05	6.37e+05
Weighted PageRank ^b	3.60e+05	3.61e+05
(C) Results for $\kappa_r/\kappa_b = 10^2$		
cond(\mathcal{A})	4.35e+03	
Strategy	cond(\mathcal{A}_{cc}^-)	cond(\mathcal{A}^+)
Mumps	4.35e+03	4.30e+03
Gravity center	4.21e+03	4.22e+03
Perron	4.21e+03	4.22e+03
Katz ^b	4.21e+03	4.22e+03
PageRank ^b	4.56e+03	4.85e+03
Weighted Perron	4.21e+03	4.22e+03
Weighted Katz ^b	4.20e+03	4.21e+03
Weighted PageRank ^b	4.21e+03	4.22e+03

When $\kappa_r/\kappa_b = 1$, the square is homogeneous and the best fixing-node is the central one which coincides with the gravity center of all mesh nodes. This central node is picked up by almost all methods. Logically, the use of the weighted graph is not useful for this homogeneous problem. An interesting point is that all PageRank variants do not select the optimal fixing-node here. As illustrated in Figure 5, all interior nodes have the same PageRank centrality and the position of the node has little impact. A similar behavior is seen on the Katz centrality but the map is slightly smoother. For Katz (with $\alpha = 0.5$), the transition between low score frontier nodes to high score interior nodes involves two band of elements. This transition depends on the parameter α and when $\alpha \rightarrow 1$, the Katz centrality becomes similar to the eigenvector centrality.

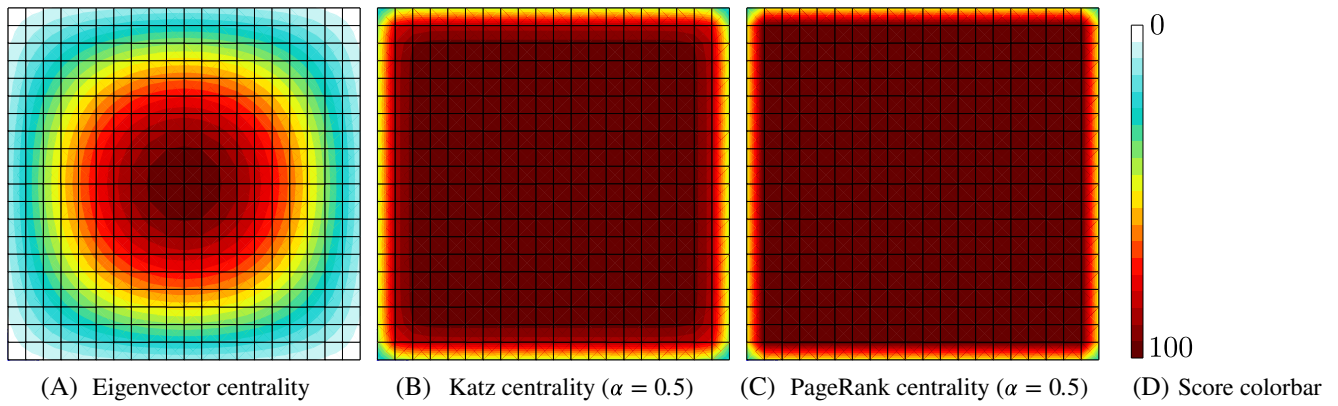


FIGURE 5 Academic thermal example: Centrality map obtained with lumped weights with $\kappa_r = \kappa_b$

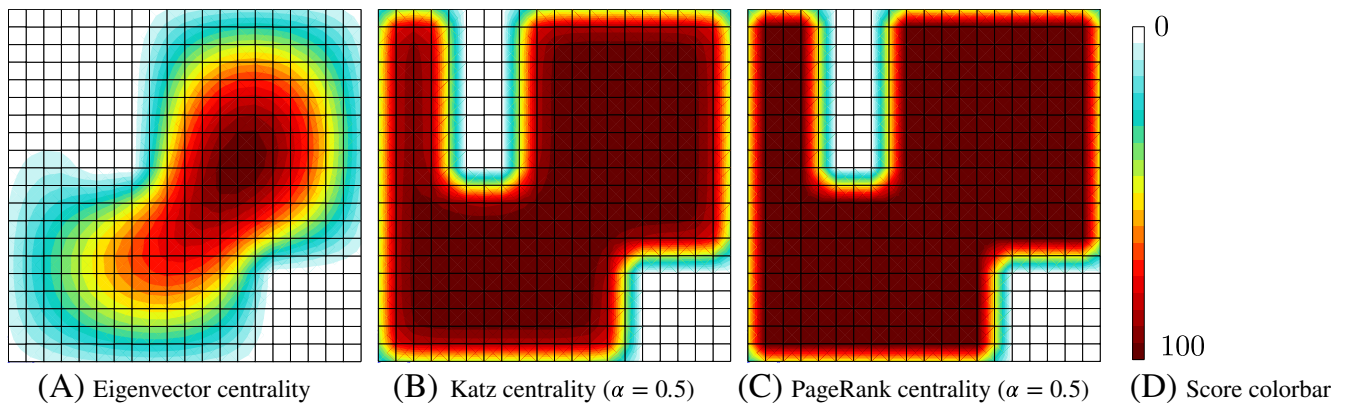


FIGURE 6 Academic thermal example: Centrality map obtained with lumped weights with $\kappa_r/\kappa_b = 10^2$

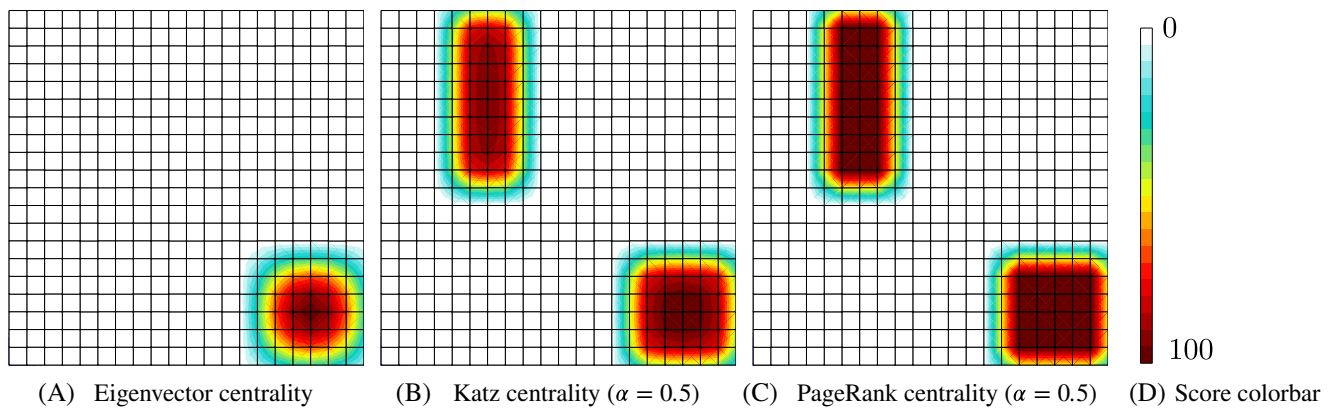


FIGURE 7 Academic thermal example: Centrality map obtained with lumped weights with $\kappa_r/\kappa_b = 10^{-2}$

When $\kappa_r/\kappa_b = 10^2$, the red central part of the square is more conductive than the blue one. The central node remains a good fixing-node candidate and the results are similar to the homogeneous case. As shown in Figure 6, the Eigenvector centrality leads to a small area with high centrality while Katz and PageRank precisely detect the high conductivity areas.

The case $\kappa_r/\kappa_b = 10^{-2}$ is more interesting. Here, the red central part of the square is less conductive than the blue one and the central node of the square is not a good fixing-node candidate. Without the use of the weighted graph, Perron, Katz and Gravity center methods still select the central node of the square. By taking into account this heterogeneity, all weighted methods provide a better fixing-node and decrease the condition numbers of both the generalized inverse and of the inner block. Due to the simplicity of the test case, the improvement of the condition number remains limited but

this behavior is promising. Again, Figure 7 plots the centrality score. Both Katz and PageRank centralities detect the two high conductivity areas while the eigenvector centrality only got the right lower one.

6.2.2 | Influence of the parameter α

The influence of the parameter α on the condition number are shown in Table 2 for the Katz centrality and in Table 3 and for the PageRank one. As can be seen in Table 2, the damping parameter α has little impact on the condition number. Almost all $\alpha \geq 0.5$ provide the same fixing-node. With $\alpha \leq 0.4$, several nodes may have the maximal score. In such a case, the node with the maximal score and the smallest rank is selected. Regarding the PageRank centrality in Table 3, results are also clustered but no clear tendency can be drawn. This little sensitivity may be due to the intrinsic part of the centrality β which is defined as the diagonal value of the matrix. It may also be reduced by the simplicity of this test case. This little sensitivity is rather beneficial since a fine tuning of the parameter alpha is not necessary.

6.3 | 3D elasticity benchmark

The thermal test case is instructive since it allows a good visualization of the various centrality maps. It remains however really simple: the mesh is regular, only one fixing-node is needed and the size of the matrix is really small. To confirm the previous results, a generalization of the 3D elasto-static solid benchmark proposed in the article³⁴ is provided in this Section. First the unit cube is discretized using a $6 \times 6 \times 6$ regular grid made with Q1 elements (c3d8). Then this unit cube is deformed using the map f

$$f : \begin{cases} [0, 1]^3 \rightarrow \mathbb{R}^3 \\ (x, y, z) \mapsto \left((x - \frac{1}{2}) \times (1 - 0.6\sqrt{z}), (y - \frac{1}{2}) \times (1 - 0.6\sqrt{z}), \sqrt{z} \right) \end{cases} .$$

As shown in Figure 8, the unit cube becomes a truncated pyramid. This truncated pyramid is made of two different isotropic linear elastic materials. Both layers share the same Poisson's coefficient 0.3 but the Young's modulus alternates between a soft value E_r and a stiff one E_b . Three values of heterogeneity ratio are considered $E_b/E_r \in \{1, 10^2, 10^3\}$. The truncated pyramid is totally floating, the defect of the associated stiffness matrix is 6. According to the rule defined in Section 4.3, four condensation nodes are used in this benchmark ($M = 4$), leading to a Schur complement S_{cc} of size 12×12 .

Again, all the proposed methods are compared and the results are gathered in Table 4. For Katz and PageRank centralities which depend on the parameter α , nine values are tested (0.1, 0.2, 0.3, 0.4, 0.5, 0.6, 0.7, 0.8, 0.9). Only the best and worst results, with respect to the value of α , are displayed. The best result (resp. worst) is marked with an exponent \square^b (resp. \square^w).

As shown in Table 4, weighted variants perform better than unweighted ones. For the homogeneous case ($E_b = E_r$), all the results are clustered. For heterogeneous problem, the weighted variants lead to a reduction of the condition number by a factor 10^2 in comparison with Mumps. The condition number is approximately reduced by a factor 10 if we compare with gravity center method or unweighted centralities. The sensitivity to the parameter α is again reduced since best and worst results are similar.

6.4 | Robustness of the kernel detection process on a simplified laminated composite

All kernel detection methods rely on thresholds which may be automatically chosen or provided by the user. The larger the admissible range, leading to a correct estimation of the kernel dimension, the more robust the method is. As pointed out in Reference 9, the admissible range becomes narrow when considering ill conditioned systems. It is possible to put in difficulty most advanced direct solvers such as MUMPS with pathological test cases. In this section, we provide such a test case and demonstrate the robustness of the proposed methods. It is a simplified version of the laminated composite proposed in a previous work.⁶

A slender heterogeneous (3D) plate with aspect ratio $20 \times 10 \times 1$ is discretized into $100 \times 50 \times 10$ regular twenty-node brick elements (c3d20) (see Figure 9). This plate is made of five thin linear elastic layers (see Figure 9A).

TABLE 2 Academic thermal example: Influence of the parameter α for weighted Katz

(A) Results for $\kappa_r/\kappa_b = 10^{-2}$		
$\overline{\text{cond}}(\mathcal{A})$	1.42e+05	
α	$\text{cond}(\mathcal{A}_{cc}^-)$	$\overline{\text{cond}}(\mathcal{A}^+)$
0.1	6.37e+05	6.37e+05
0.2	6.37e+05	6.37e+05
0.3	6.37e+05	6.37e+05
0.4	6.37e+05	6.37e+05
0.5	6.37e+05	6.37e+05
0.6	6.37e+05	6.37e+05
0.7	6.37e+05	6.37e+05
0.8	6.37e+05	6.37e+05
0.9	6.37e+05	6.37e+05
(B) Results for $\kappa_r/\kappa_b = 10^0$		
$\overline{\text{cond}}(\mathcal{A})$	1.87e+02	
α	$\text{cond}(\mathcal{A}_{cc}^-)$	$\overline{\text{cond}}(\mathcal{A}^+)$
0.1	1.25e+03	1.30e+03
0.2	1.30e+03	1.37e+03
0.3	1.25e+03	1.30e+03
0.4	1.12e+03	1.13e+03
0.5	1.10e+03	1.11e+03
0.6	1.10e+03	1.10e+03
0.7	1.10e+03	1.10e+03
0.8	1.10e+03	1.10e+03
0.9	1.10e+03	1.10e+03
(C) Results for $\kappa_r/\kappa_b = 10^2$		
$\overline{\text{cond}}(\mathcal{A})$	3.88e+03	
α	$\text{cond}(\mathcal{A}_{cc}^-)$	$\overline{\text{cond}}(\mathcal{A}^+)$
0.1	4.20e+03	4.21e+03
0.2	4.26e+03	4.27e+03
0.3	4.24e+03	4.26e+03
0.4	4.24e+03	4.26e+03
0.5	4.24e+03	4.26e+03
0.6	4.24e+03	4.26e+03
0.7	4.24e+03	4.26e+03
0.8	4.23e+03	4.24e+03
0.9	4.23e+03	4.24e+03

TABLE 3 Academic thermal example: Influence of the parameter α for weighted PageRank

(A) Results for $\kappa_r/\kappa_b = 10^{-2}$		
$\overline{\text{cond}}(\mathcal{A})$	1.42e+05	
α	$\text{cond}(\mathcal{A}_{cc}^-)$	$\overline{\text{cond}}(\mathcal{A}^+)$
0.1	3.60e+05	3.61e+05
0.2	3.61e+05	3.61e+05
0.3	3.61e+05	3.61e+05
0.4	3.63e+05	3.64e+05
0.5	3.60e+05	3.61e+05
0.6	3.62e+05	3.62e+05
0.7	3.62e+05	3.63e+05
0.8	3.61e+05	3.61e+05
0.9	3.61e+05	3.61e+05
(B) Results for $\kappa_r/\kappa_b = 10^0$		
$\overline{\text{cond}}(\mathcal{A})$	1.87e+02	
α	$\text{cond}(\mathcal{A}_{cc}^-)$	$\overline{\text{cond}}(\mathcal{A}^+)$
0.1	1.37e+03	1.45e+03
0.2	1.30e+03	1.37e+03
0.3	1.89e+03	3.14e+03
0.4	1.89e+03	2.54e+03
0.5	1.69e+03	1.51e+03
0.6	1.25e+03	1.30e+03
0.7	1.78e+03	1.92e+03
0.8	1.69e+03	1.51e+03
0.9	1.81e+03	2.33e+03
(C) Results for $\kappa_r/\kappa_b = 10^2$		
$\overline{\text{cond}}(\mathcal{A})$	3.88e+03	
α	$\text{cond}(\mathcal{A}_{cc}^-)$	$\overline{\text{cond}}(\mathcal{A}^+)$
0.1	4.56e+03	4.85e+03
0.2	4.27e+03	4.29e+03
0.3	4.56e+03	4.85e+03
0.4	4.21e+03	4.22e+03
0.5	4.56e+03	4.85e+03
0.6	4.56e+03	4.85e+03
0.7	4.91e+03	5.10e+03
0.8	4.56e+03	4.85e+03
0.9	4.56e+03	4.85e+03

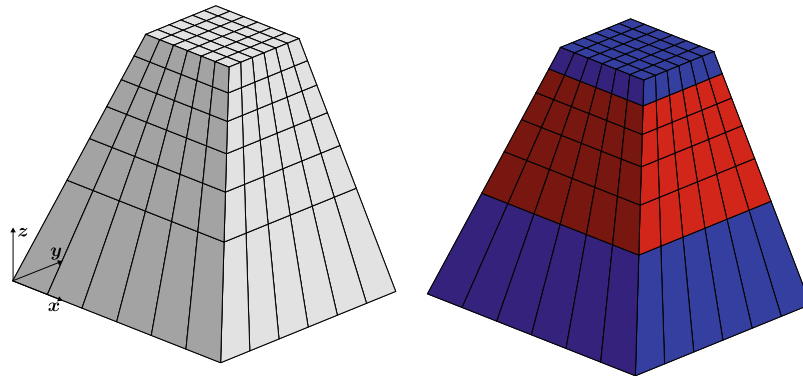


FIGURE 8 Solid benchmark: the solid is made of two different material with Young modulus E_r (resp. E_b) for the red (resp. blue) part. Inspired by Brzobohatý et al.³⁴

All layers are made with isotropic linear elastic materials. They share the same Poisson's coefficient 0.3 but the Young's modulus alternates between a soft value E_r and a stiff one E_b . This case aims at representing a laminated composite material made out of a soft material reinforced by a stiffer one. Six values of heterogeneity ratio are considered $E_b/E_r \in \{10^2, 10^3, 10^4, 10^5, 10^6\}$.

In order to solve the problem with FETI-like methods, the mesh is split into 16 domains (see Figure 9A) composed on average of 3100 elements and 45,000 degrees of freedom. The decomposition is generated with the Scotch graph partitioning library.⁵⁵ With this decomposition, there is only one subdomain in the thickness. The laminated composite is solicited like a cantilever beam, so most of the subdomains are totally floating, the defect of the corresponding local stiffness operators is six. Also, stiffness operators are ill conditioned due to the bad subdomain aspect ratio and the jump of material coefficient. In the following, we only consider the (totally floating) red subdomain of Figure 9. Similar results are obtained for all floating subdomains.

6.4.1 | Kernel detection with MUMPS 5.3.5

There are two user defined parameters, CNTL(1) and CNTL(3), for the detection of the kernel dimension in MUMPS 5.3.5. The control parameter CNTL(1) is a relative threshold for numerical pivoting. The default value $\text{CNTL}(1) = 1e-2$ is used in this work. The second control parameter CNTL(3) is a threshold to detect null pivots. According to the documentation, a pivot is considered to be null if the infinite norm of its row/column is smaller than a threshold $thres$. The default value of $\text{CNTL}(3) = 0$ provides an automatic process to determines this threshold, $thres = \epsilon \times 10^{-5} \times \|A_{pre}\|$ where A_{pre} is the preprocessed matrix to be factorized and ϵ is machine precision. A positive value of CNTL(3) leads to the user defined threshold $thres = \text{CNTL}(3) \times \|A_{pre}\|$.

The result of the kernel detection procedure is shown in Table 5. Whatever the heterogeneity, the automatic threshold does not detect the right kernel size. With a user defined threshold, it is possible to recover the right kernel one. However, the admissible range for CNTL(3) decreases when considering high heterogeneity. The validity range for the case $E_b/E_r = 1e+6$ is less than two decades.

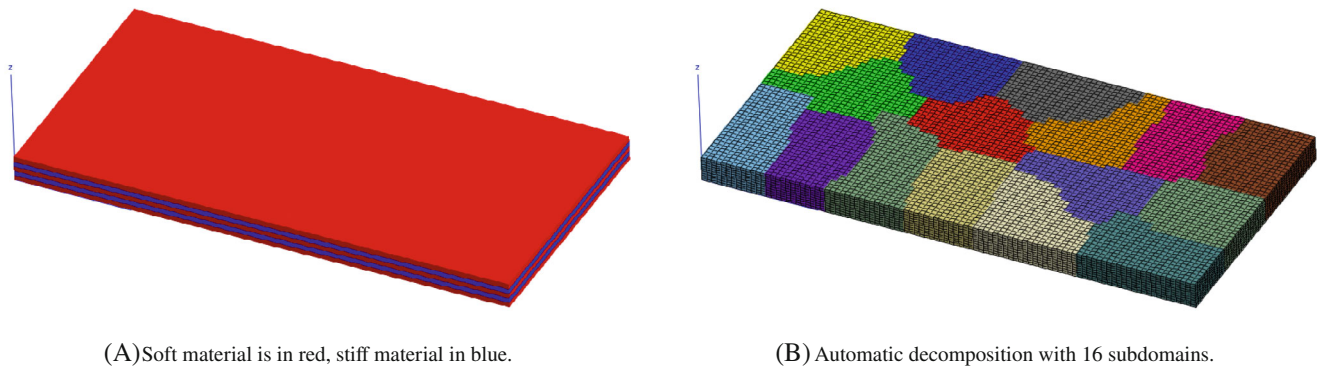
6.4.2 | Gravity center based method

The gravity center selection strategy is applied to the same totally unrestrained subdomain. Four condensation nodes are used in this benchmark, leading to a Schur complement S_{cc} of size 12×12 . In order to investigate the robustness of the method, the singular values of the Schur complement are shown in Figure 10. The validity range of the threshold ϵ for the Relative criterion (11) and Jump criterion (12) can be obtained with this graph. The gravity center is always in the central soft layer of the composite because of the symmetry of the problem. The validity range of the threshold is much wider than previously but the increase of the heterogeneity ratio E_b/E_r reduces it by the same proportion.

TABLE 4 Solid benchmark: Comparison of all methods

(A) Results for $E_b = E_r$		
$\overline{\text{cond}}(\mathcal{A})$	7.82e+04	
Strategy	$\text{cond}(\mathcal{A}_{cc}^-)$	$\overline{\text{cond}}(\mathcal{A}^+)$
Mumps	7.82e+04	7.79e+04
Gravity center	3.81e+03	3.08e+03
Perron	4.52e+03	4.48e+03
Katz ^b	4.52e+03	4.48e+03
Katz ^w	4.52e+03	4.48e+03
PageRank ^b	4.31e+03	4.22e+03
PageRank ^w	4.60e+04	4.35e+04
Weighted Perron	2.86e+03	2.67e+03
Weighted Katz ^b	2.86e+03	2.67e+03
Weighted Katz ^w	4.58e+03	4.49e+03
Weighted PageRank ^b	5.64e+03	5.50e+03
Weighted PageRank ^w	6.74e+03	6.68e+03
(B) Results for $E_b/E_r = 10^2$		
$\overline{\text{cond}}(\mathcal{A})$	6.52e+06	
Strategy	$\text{cond}(\mathcal{A}_{cc}^-)$	$\overline{\text{cond}}(\mathcal{A}^+)$
Mumps	6.52e+06	5.96e+06
Gravity center	1.52e+05	5.05e+04
Perron	2.73e+05	2.49e+05
Katz ^b	2.73e+05	2.49e+05
Katz ^w	2.73e+05	2.49e+05
PageRank ^b	9.17e+04	6.39e+04
PageRank ^w	3.19e+05	2.97e+05
Weighted Perron	3.46e+04	3.09e+04
Weighted Katz ^b	3.46e+04	3.09e+04
Weighted Katz ^w	3.96e+04	3.14e+04
Weighted PageRank ^b	5.16e+04	3.27e+04
Weighted PageRank ^w	8.70e+04	4.76e+04
(C) Results for $E_b/E_r = 10^3$		
$\overline{\text{cond}}(\mathcal{A})$	6.56e+07	
Strategy	$\text{cond}(\mathcal{A}_{cc}^-)$	$\overline{\text{cond}}(\mathcal{A}^+)$
Mumps	6.56e+07	5.93e+07
Gravity center	1.49e+06	4.80e+05
Perron	2.70e+06	2.44e+06
Katz ^b	2.70e+06	2.44e+06
Katz ^w	2.70e+06	2.44e+06
PageRank ^b	8.82e+05	5.47e+05
PageRank ^w	2.49e+06	2.21e+06
Weighted Perron	3.42e+05	2.94e+05
Weighted Katz ^b	3.42e+05	2.94e+05
Weighted Katz ^w	3.88e+05	2.92e+05
Weighted PageRank ^b	4.99e+05	2.88e+05
Weighted PageRank ^w	8.31e+05	3.99e+05

Note: For Katz and PageRank only the best and worst results are shown.



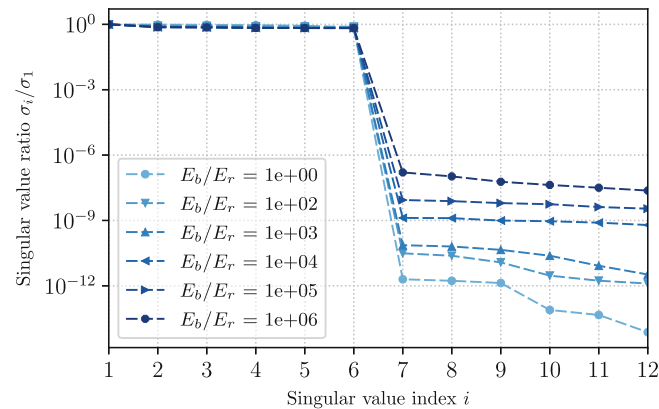
(A) Soft material is in red, stiff material in blue.

(B) Automatic decomposition with 16 subdomains.

FIGURE 9 Heterogeneous composite

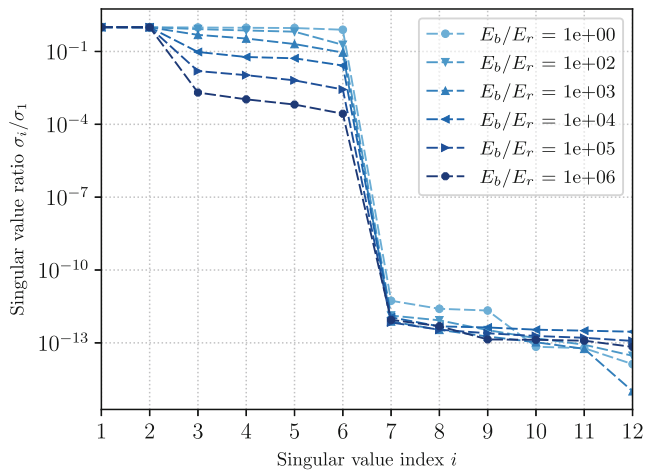
TABLE 5 Laminated composite, red subdomain of Figure 9: Dependency of kernel detection with respect to MUMPS parameter

E_b/E_r	Threshold for null pivots by CNTL(3)						Automatic
	1e-03	1e-04	1e-05	1e-06	1e-07	1e-08	
1e+02	6	6	6	6	6	6	0
1e+03	6	6	6	6	6	5	0
1e+04	6	6	6	6	4	3	0
1e+05	7	6	6	5	5	3	0
1e+06	9	6	5	4	3	3	0

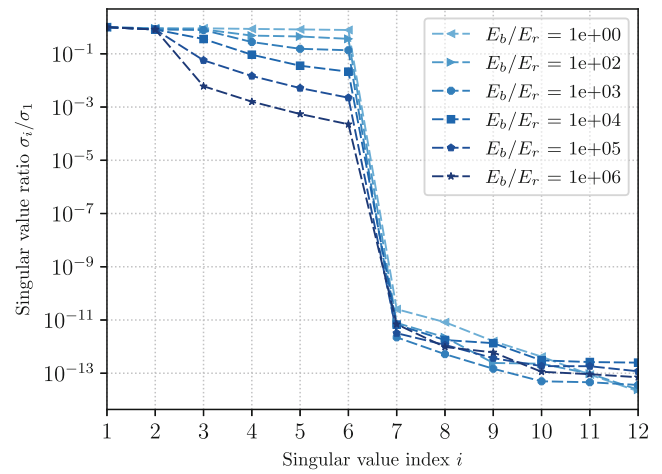
FIGURE 10 Laminated composite: Singular values of the Schur complement \mathcal{S}_{cc} for the gravity center variant. Four condensation nodes are used. Whatever the weight used, the method always selects node in the central layer made of soft material

6.4.3 | Graph based methods

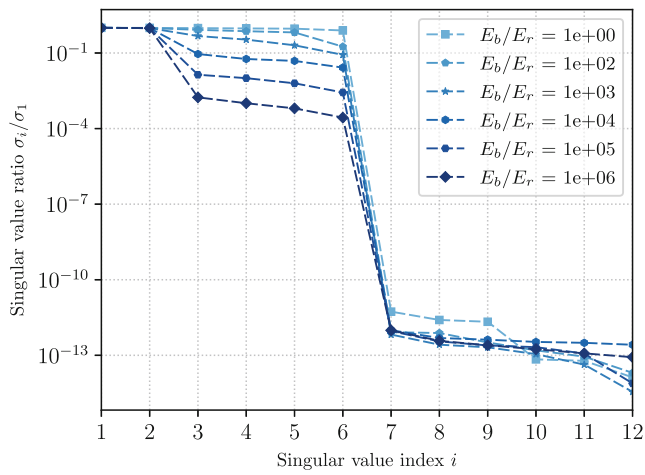
The graph based kernel detection methods are applied to the same totally unrestrained subdomain. Again, the singular values of the Schur complement selected by the Katz and Page Rank (with four fixing-nodes) are shown in Figure 11. The lumped weight is used for both methods and three damping values are considered $\alpha \in (0.3, 0.5, 0.9)$. As shown in Figure 11, whatever the heterogeneity ratio E_b/E_r , the singular values associated with the six rigid body motions are easily recognizable. For all cases, the admissible range for the selection threshold covers at least five decades. The PageRank variants with $\alpha \in (0.5, 0.9)$ behave really well since the threshold validity range is insensitive to the material heterogeneity.



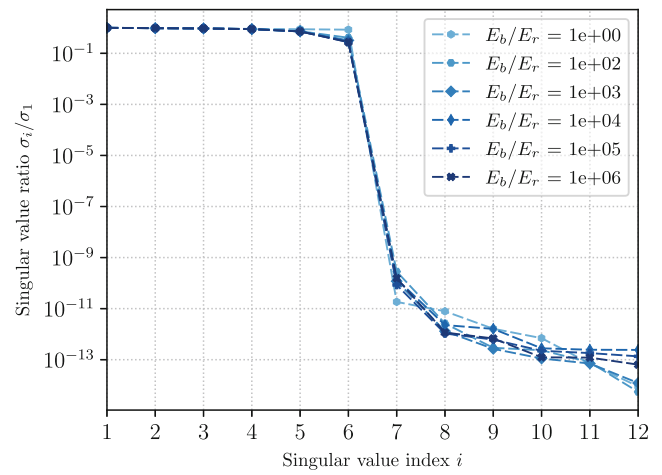
(A) Katz with damping parameter $\alpha = 0.3$.



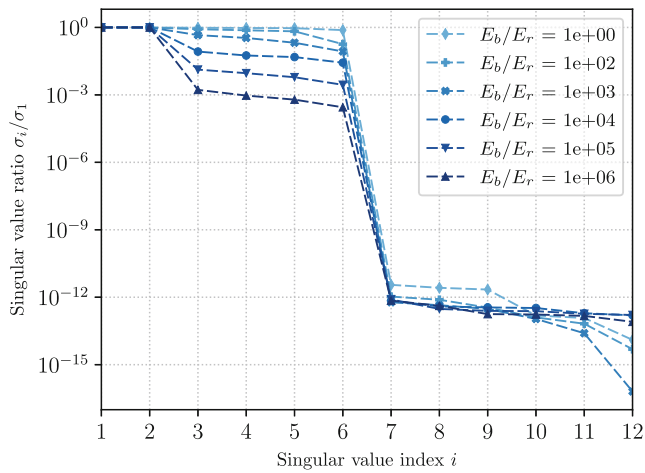
(B) Page Rank with damping parameter $\alpha = 0.3$.



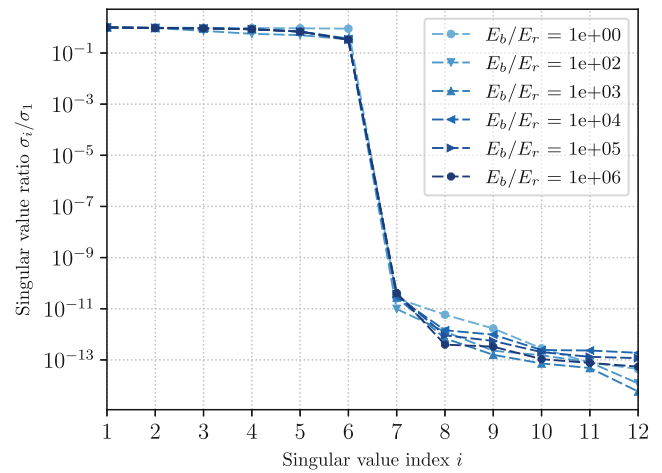
(C) Katz with damping parameter $\alpha = 0.5$.



(D) Page Rank with damping parameter $\alpha = 0.5$.



(E) Katz with damping parameter $\alpha = 0.9$.



(F) Page Rank with damping parameter $\alpha = 0.9$.

FIGURE 11 Laminated composite: Singular values of the Schur complement S_{cc} for Katz and Page Rank. Four condensation nodes are used with lumped weight

About the computational cost

With a local problem of approximately 45,000 degrees of freedom, the laminated composite example is large enough to investigate the computational times. Results are similar whatever the heterogeneity and the value of the parameter α , so only the case $E_b/E_r = 1e + 2$ and $\alpha = 0.5$ are shown. Only one core is used to facilitate the comparison so colors are processed successively. Table 6 compares the computational time distributions obtained with the various methods. It corresponds to the time spent to compute the generalized inverse and the nullspace. Two timers have been defined:

- The *MUMPS internal* timer represents the time spent computing the (partial) factorization and (partial) solves with MUMPS.
- The *Total selection* timer regroups the time spent selecting the fixing-nodes. This timer is split into three subcategories. The *Split* timer is the time spent in the virtual split. The time spent in building (15) or (16) corresponds to the *System build* timer. Finally, the *Resolution* timer accounts for the resolution of (15) or (16).

As shown in Table 6, the selection of the fixing-nodes only represents few percent of the whole computation. The most costly part in the selection process is the construction of the Katz and PageRank linear systems. It was expected since this timer includes the costly computation of the edge weights. Due to the overhead associated with the selection process, graph based methods are slightly slower than directly using the MUMPS solver. The time spent in MUMPS is also slightly higher when partial factorizations are used.

Impact of the kernel misdetection on the FETI convergence and solution

As discussed in Section 4.3, the detection of local operators nullspaces is a crucial point of the FETI method. If the nullspace is misdetected the FETI method diverges and/or leads to a wrong solution. To illustrate this point, the FETI method is applied to the laminated composite example with $E_b/E_r = 10^6$. Both the preconditioner and the saddle-point projector are equipped with the Dirichlet local operator and the stiffness scaling (see for instance⁵⁶ for the corresponding definitions). In this test case, the left surface of the plate is clamped while a vertical displacement u_z is prescribed on the right surface. There are 72 rigid body modes ($3 \times 0 + 10 \times 6 + 3 \times 4$) with the domain decomposition shown in Figure 9A. Figure 12 shows the convergence curves of the Conjugate Gradient of the FETI method.

TABLE 6 Laminated composite: Distribution of the computational time for MUMPS, Katz and Page Rank

	Total	MUMPS internal	Fixing-nodes selection			
			Total selection	Split	System build	Resolution
Mumps	2.72s	2.72s (100%)				
Katz	3.01s	2.79s (93%)	0.22s (7%)	0.01s	0.12s	0.09s
PageRank	3.03s	2.79s (92%)	0.24s (8%)	0.01s	0.14s	0.09s

Note: Four condensation nodes are used with lumped weight.

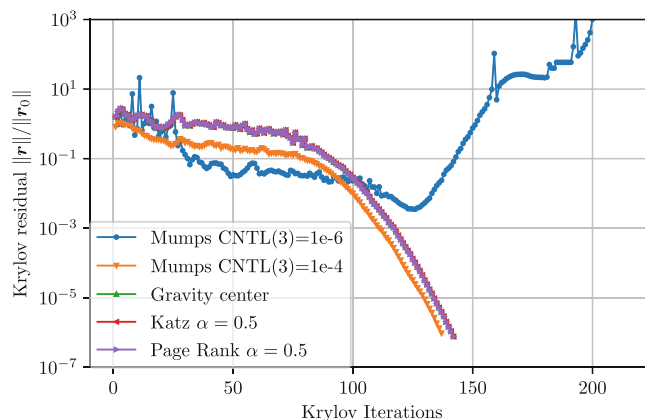


FIGURE 12 Convergence curves for the laminated composite example with $E_b/E_r = 10^6$. The FETI solver is equipped with a Dirichlet preconditioner and stiffness scaling. The saddle-point projector also use the Dirichlet operator with the stiffness scaling. The left surface of the plate is clamped while a vertical displacement u_z is prescribed on the right surface

Katz, Page Rank and Gravity center variants correctly detect the 72 rigid body modes. For this test case, they lead to the same convergence curve and solution. At convergence, the finite element residual is $\|\mathbf{Ku} - \mathbf{f}\|/\|\mathbf{f}\| = 1.229e - 9$ (the right-hand-side \mathbf{f} is not null because of the prescribed Dirichlet boundary conditions). The vertical displacement is shown in Figure 13. This solution will serve as reference.

With Mumps as local solver, there is not a unique value of CNTL(3) working for all subdomains. For instance, with $\text{CNTL}(3) = 1e-6$, the number of rigid body modes is largely underestimated: 41 rigid body modes are detected ($3 \times 0 + 1 \times 2 + 9 \times 3 + 3 \times 4$). As can be seen in Figure 12, the Conjugate Gradient clearly diverges. With $\text{CNTL}(3) = 1e-4$, the number of rigid body modes is close to the exact one: 73 rigid body modes are detected ($3 \times 0 + 9 \times 6 + 1 \times 7 + 3 \times 4$). Here, the Conjugate Gradient is convergent. However, it leads to a wrong solution as shown in Figure 14. At convergence, the finite element residual $\|\mathbf{Ku} - \mathbf{f}\|/\|\mathbf{f}\| = 4.676$ is quite large that indicates that the system solved by the FETI method is not equivalent anymore to the original one.

7 | APPLICATION TO ENGINEERING PROBLEMS: NUMERICAL HOMOGENIZATION OF THE MECHANICAL BEHAVIOR OF SOLID PROPELLANTS

Solid propellants are energetic materials composed of an organic matrix and numerous metallic inclusions. This type of material brings several space scales into play because of the large dispersion of the particles sizes. The numerical homogenization of this type of material involves the simulation of a Representative Volume Element (RVE) with a large number of unknowns. Iterative solvers are essential whereas they are put to the test by the condition number of the linear systems.

Indeed, the material is highly heterogeneous, the jump in Young modulus between the matrix and the metallic inclusions is approximately 10^5 . Because of the high density of inclusions in the RVE, heterogeneity is very frequently misplaced with respect to the domain decomposition interface. Also, elements of the mesh of the matrix that are located between two close inclusions often exhibit poor quality factors which degrade even more the condition number of the linear system to be solved. Finally, the organic matrix is almost incompressible. If a linear elastic behavior is assumed for the matrix, the

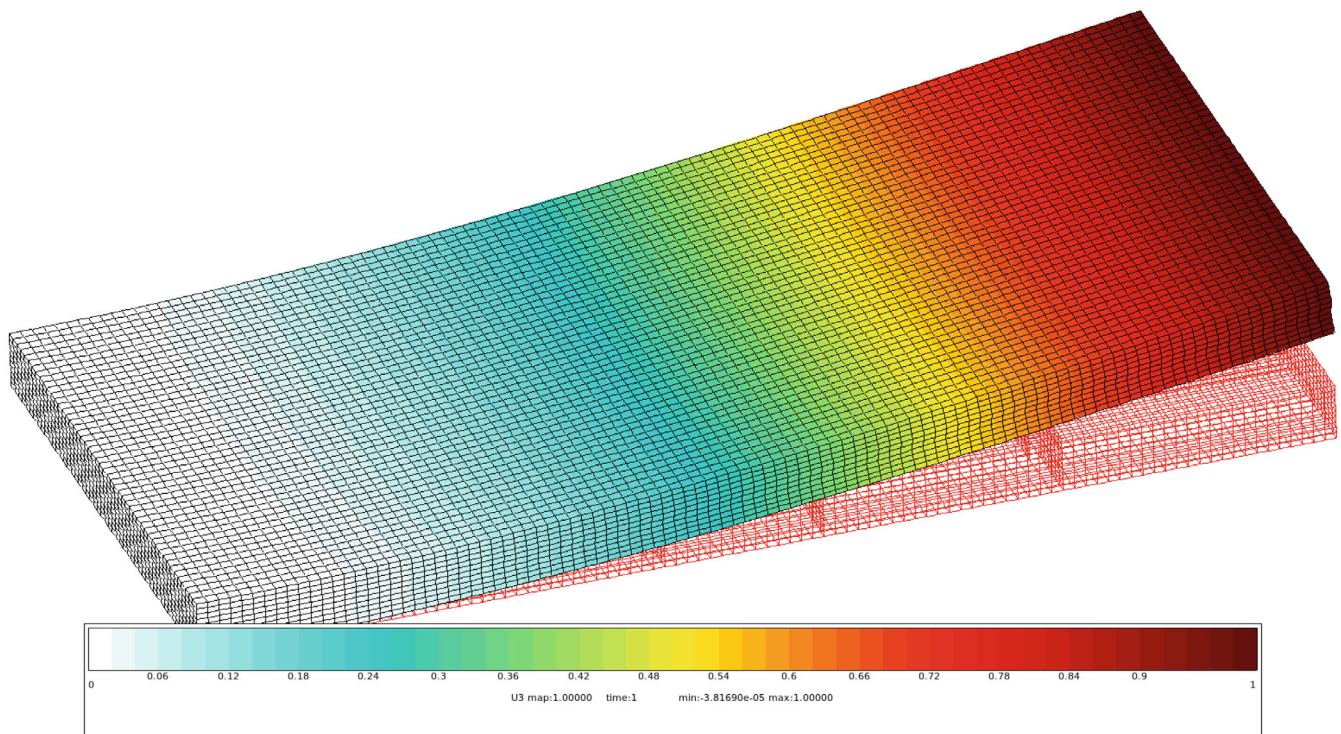


FIGURE 13 Vertical displacement u_z obtained at convergence with the Gravity center variant. The same results hold for Katz and Page Rank. Displacements are magnified by a factor 2

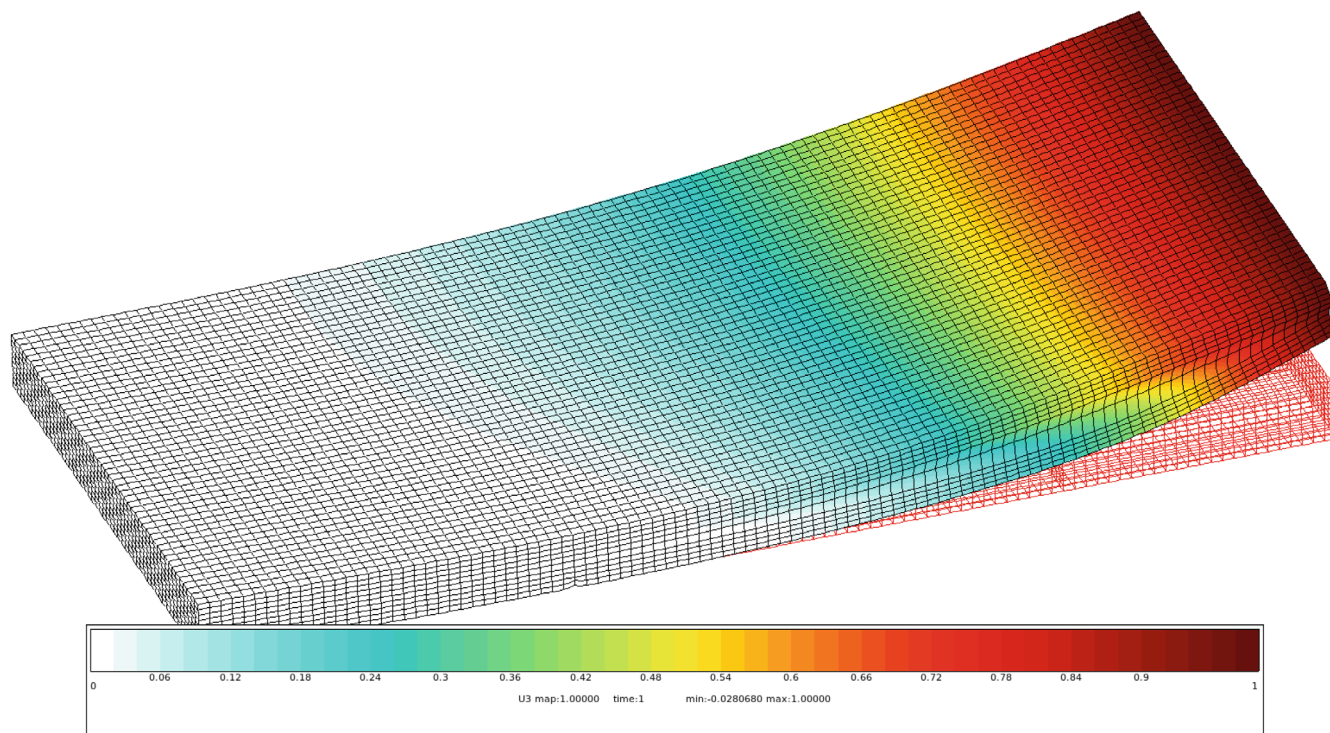


FIGURE 14 Vertical displacement u_z obtained at convergence with the Mumps variant and $\text{CNTL}(3) = 1\text{e-}4$. Displacements are magnified by a factor 2

Poisson coefficient is 0.499 such that mixed pressure–displacement–volume variation finite element needs to be used (see Sections 2.6 and 5.5 in Reference 45). For simplicity, the geometrically linearized problem is considered. This assumption has little impact on the conclusion of the study. In the case of the finite strain model, the kernel detection and generalized inverse computation are applied to the tangent system.

Domain decomposition methods, such as the FETI method and its derivatives are strongly impacted by the numerical difficulties. This is typically a case where the multipreconditioned variant AMPFETI is needed. A robust process to detect local operators nullspaces and to compute generalized inverse is also essential. The finite element mesh, the domain decomposition for one distribution of particles and the results obtained in a previous work⁸ are shown in Figure 15. The finite element mesh contains 5,494,528 quadratic tetrahedrons and the global system has 22 millions of degrees of freedom; 448 subdomains are used for the partitioning. The decomposition is generated with Scotch. The RVE is submitted to hydrostatic compression. This load is prescribed as a uniform normal displacement on the external faces of the RVE. Under hydrostatic compression, only the normal displacement of the external surface of the RVE is constrained.

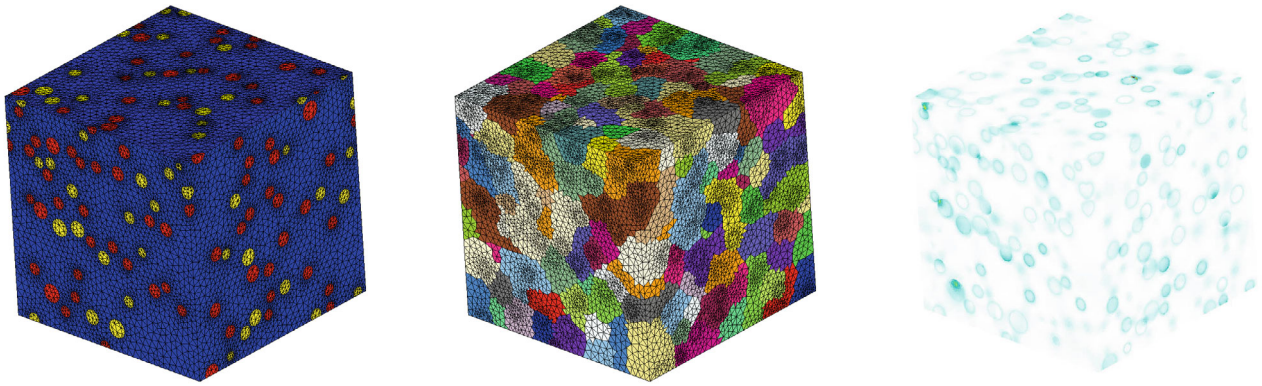
The Von Mises stress field is shown in Figure 15C for a hydrostatic compression load. The focus is carried on the two typical subdomains shown in Figure 16. The first one is in the bulk of the RVE. This subdomain is totally floating and possesses six rigid body motions. The second one is close to a boundary so this subdomain is partially constrained and has only three rigid body motions.

7.1 | Short reminder on three field mixed elements

This section quickly recall the theory of three field mixed elements, more details can be found for example in Sections 2.6 and 5.5 in the reference book.⁴⁵ The treatment of nearly incompressible materials is considered by splitting the stress and strain into their deviatoric and spherical parts. The linearized strain $\boldsymbol{\varepsilon}$ is expressed in the mixed form

$$\boldsymbol{\varepsilon} = \mathbf{I}_{dev} : \nabla^s \mathbf{u} + \frac{1}{3} \theta \mathbf{1} \quad (17)$$

where \mathbf{u} is the displacement and θ is the volume variation. Classically, $\nabla^s \mathbf{u}$ is the symmetrized displacement gradient and $\mathbf{1}$ is the second order identity tensor. The fourth-order tensor \mathbf{I}_{dev} is a projection operator mapping a symmetric

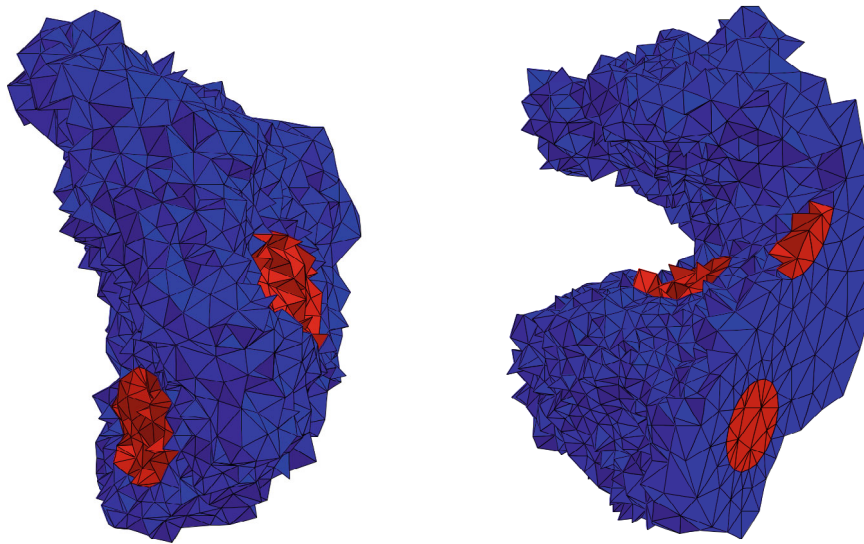


(A) Finite element mesh of the RVE, the red and yellow colors correspond to two different types of inclusions.

(B) Domain decomposition in 448 subdomains.

(C) Von Mises stress field, the white color characterises low stresses area.

FIGURE 15 Numerical homogenization of the mechanical behavior of solid propellants



(A) Typical aspect of a subdomain in the bulk of the RVE. This subdomain is totally unrestrained.

(B) Typical aspect of a subdomain close to a boundary. This subdomain is partially constrained by the boundary condition (hydrostatic compression).

FIGURE 16 Solid propellants: typical aspect of subdomain meshes

second-order tensor into its deviatoric part, such that $\mathbf{I}_{dev} : \nabla^s \mathbf{u} = \nabla^s \mathbf{u} - \frac{1}{3} \text{trace}(\nabla^s \mathbf{u}) \mathbf{1}$. Similarly the fourth-order tensor \mathbf{I}_{vol} is defined, it maps a symmetric second-order tensor into its volumetric part, such that $\mathbf{I}_{vol} : \nabla^s \mathbf{u} = \frac{1}{3} \text{trace}(\nabla^s \mathbf{u}) \mathbf{1}$. The stresses are also expressed in a mixed form as

$$\boldsymbol{\sigma} = \mathbf{I}_{dev} : \bar{\boldsymbol{\sigma}} + p \mathbf{1} \quad (18)$$

where p is the pressure and $\bar{\boldsymbol{\sigma}}$ is the stresses deduced from the constitutive model $\bar{\boldsymbol{\sigma}} = \boldsymbol{\sigma}(\boldsymbol{\epsilon})$. Assuming quasi-static problem, the weak form is given by

$$\begin{aligned} \int_{\Omega} \delta \nabla^s \mathbf{u} : \boldsymbol{\sigma} \, d\Omega &= \int_{\Omega} \delta \mathbf{u} \cdot \mathbf{b} \, d\Omega + \int_{\partial\Omega} \delta \mathbf{u} \cdot \mathbf{t} \, d\Gamma \\ \int_{\Omega} \delta p (\mathbf{I}_{vol} : \nabla^s \mathbf{u} - \theta) \, d\Omega &= 0 \\ \int_{\Omega} \delta \theta (\mathbf{I}_{vol} : \bar{\boldsymbol{\sigma}} - p) \, d\Omega &= 0 \end{aligned} \quad (19)$$

where \mathbf{b} and \mathbf{t} are body and traction forces, respectively. The virtual quantities are denoted $\delta \mathbf{u}$, δp and $\delta \theta$. The finite element approximations are given by $\mathbf{u} \approx \mathbf{N}_u \{\mathbf{u}\}$, $p \approx \mathbf{N}_p \{p\}$ and $\theta \approx \mathbf{N}_\theta \{\theta\}$. The same approximation is chosen for the virtual quantities. The Voigt notation for the strain and stress tensors are denoted, $\{\boldsymbol{\varepsilon}\}$ and $\{\boldsymbol{\sigma}\}$. With the notation $\mathbf{m} = \{1 \ 1 \ 1 \ 0 \ 0 \ 0\}^\top$, the matrix form of the deviatoric projector is $\mathbf{I}_d = \mathbf{I} - \frac{1}{3} \mathbf{m} \mathbf{m}^\top$. The strain and stresses are given by

$$\begin{aligned} \{\boldsymbol{\varepsilon}\} &= \mathbf{I}_d \mathbf{B} \{\mathbf{u}\} + \frac{1}{3} \mathbf{m} \mathbf{N}_\theta \{\theta\} \\ \{\boldsymbol{\sigma}\} &= \mathbf{I}_d \{\bar{\boldsymbol{\sigma}}\} + \mathbf{m} \mathbf{N}_p \{p\} \end{aligned} \quad (20)$$

where \mathbf{B} is the standard strain-displacement matrix. In order to obtain the tangent system, the constitutive equation is linearized

$$\{d\bar{\boldsymbol{\sigma}}\} = \mathbf{D}_T \{d\boldsymbol{\varepsilon}\} \quad (21)$$

where $\{d\boldsymbol{\varepsilon}\}$ is the mixed strain variation and \mathbf{D}_T is the tangent modulus. Finally, the tangent system is obtained

$$\mathbf{K}^{up\theta} = \begin{bmatrix} \mathbf{K}_{uu} & \mathbf{K}_{u\theta} & \mathbf{K}_{up} \\ \mathbf{K}_{\theta u} & \mathbf{K}_{\theta\theta} & -\mathbf{K}_{\theta p} \\ \mathbf{K}_{pu} & -\mathbf{K}_{p\theta} & \mathbf{0} \end{bmatrix} \quad (22)$$

with

$$\begin{aligned} \mathbf{K}_{uu} &= \int_{\Omega} \mathbf{B}^\top \bar{\mathbf{D}}_{11} \mathbf{B} d\Omega & \mathbf{K}_{\theta p} &= \int_{\Omega} \mathbf{N}_\theta^\top \mathbf{N}_p d\Omega = \mathbf{K}_{p\theta}^\top \\ \mathbf{K}_{\theta\theta} &= \int_{\Omega} \mathbf{N}_\theta^\top \bar{\mathbf{D}}_{22} \mathbf{N}_\theta d\Omega & \mathbf{K}_{pu} &= \int_{\Omega} \mathbf{N}_p^\top \mathbf{m}^\top \mathbf{B} d\Omega = \mathbf{K}_{up}^\top \\ & & \mathbf{K}_{\theta u} &= \int_{\Omega} \mathbf{N}_\theta^\top \bar{\mathbf{D}}_{21} \mathbf{B} d\Omega = \mathbf{K}_{u\theta}^\top \end{aligned} \quad (23)$$

In (23), the modified constitutive tangent matrix are used to be expressed with respect to $d\mathbf{u}$ and $d\theta$

$$\begin{aligned} \bar{\mathbf{D}}_{11} &= \mathbf{I}_d \mathbf{D}_T \mathbf{I}_d & \bar{\mathbf{D}}_{12} &= \mathbf{I}_d \mathbf{D}_T \left(\frac{1}{3} \mathbf{m} \right) \\ \bar{\mathbf{D}}_{22} &= \left(\frac{1}{3} \mathbf{m}^\top \right) \mathbf{D}_T \left(\frac{1}{3} \mathbf{m} \right) & \bar{\mathbf{D}}_{21} &= \left(\frac{1}{3} \mathbf{m}^\top \right) \mathbf{D}_T \mathbf{I}_d \end{aligned} \quad (24)$$

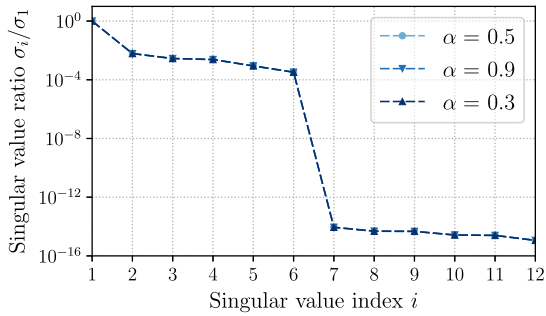
The choice of the interpolation for \mathbf{u} , p , θ is constrained by the LBB-conditions.⁵³ In the following, we consider only two types of tetrahedral elements, the first one, denoted P2P0P0 uses a continuous quadratic interpolation for \mathbf{u} and piecewise constant interpolation for p and θ . The second one, denoted P2P1P1 employs a continuous quadratic interpolation for \mathbf{u} and linear continuous interpolation for p and θ .

7.2 | Results with P2P0P0 elements

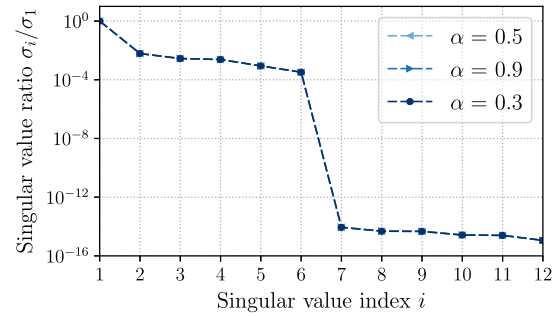
With P2P0P0 elements, the pressure and volume variation are taken locally in each element and since $\mathbf{N}_p = \mathbf{N}_\theta$, $\mathbf{K}_{p\theta}$ is symmetric positive definite. Both p and θ can be eliminated by static condensation. The modified stiffness matrix $\tilde{\mathbf{K}}^u$ is symmetric positive definite but remains ill conditioned.

$$\tilde{\mathbf{K}}^u = (\mathbf{K}_{uu} - \mathbf{K}_{u\theta} \mathbf{K}_{\theta\theta}^{-1} \mathbf{K}_{\theta u}) + (\mathbf{K}_{up} + \mathbf{K}_{u\theta} \mathbf{K}_{\theta\theta}^{-1} \mathbf{K}_{\theta p}) (\mathbf{K}_{p\theta} \mathbf{K}_{\theta\theta}^{-1} \mathbf{K}_{\theta p})^{-1} (\mathbf{K}_{pu} + \mathbf{K}_{p\theta} \mathbf{K}_{\theta\theta}^{-1} \mathbf{K}_{\theta u}) \quad (25)$$

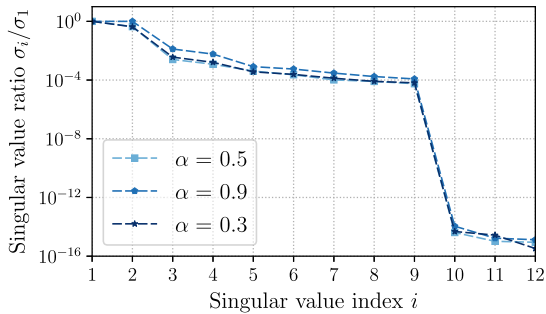
The graph based kernel detection methods are applied to the subdomains shown in Figure 16. The lumped weight is used for both methods and three damping values are considered $\alpha \in (0.3, 0.5, 0.9)$. Only four condensation nodes are used in this benchmark, leading to Schur complements \mathbf{S}_{cc} of size 12×12 . The singular values of the Schur complement selected by the weighted Katz and Page Rank strategies are shown in Figure 17. For both methods and whatever the damping values considered, the six null singular values are easily recognizable for the totally floating subdomain. For the partially



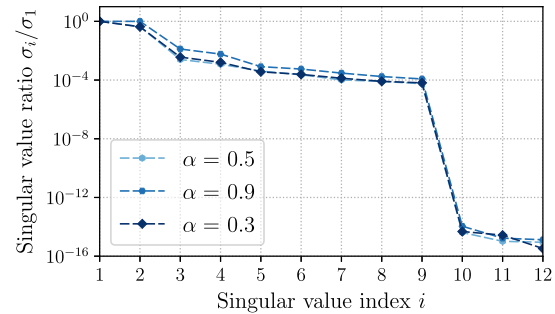
(A) Katz method for a floating subdomain (exact kernel size is 6).



(B) Page Rank method for a floating subdomain (exact kernel size is 6).



(C) Katz method for a partially floating subdomain (exact kernel size is 3).



(D) Page Rank method for a partially floating subdomain (exact kernel size is 3).

FIGURE 17 Solid propellant with P2P0P0 elements: Singular values of the Schur complement \mathbf{S}_{cc} for Katz and Page Rank. Four condensation nodes are used with lumped weight

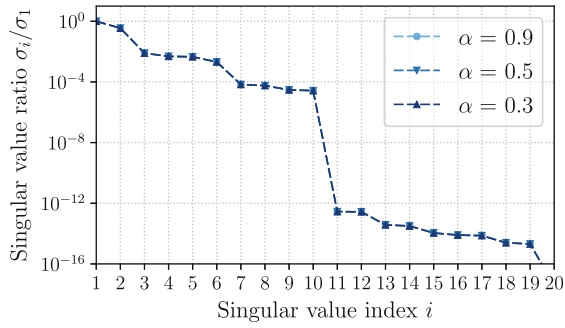
constrained subdomain, a uniform normal displacement is prescribed on the external surface of the RVE. Three rigid body motions are possible corresponding to a planar motion (two translations and one rotation in the plane of the external surface). The three null singular values corresponding to these three rigid body motions are also well clustered.

7.3 | Results with P2P1P1 elements

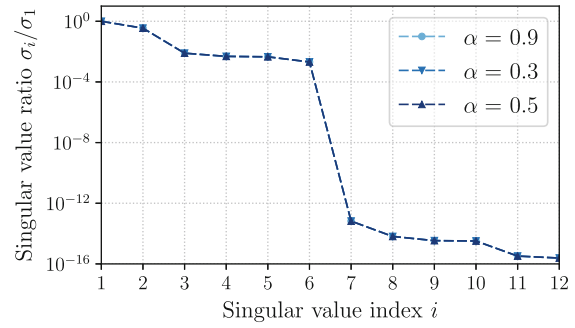
Here, the displacement is interpolated with quadratic shape functions while the pressure and volumic change are continuous and interpolated with linear shape functions. This approximation leads to a symmetric highly indefinite stiffness operator. For such problems, the difference between singular values associated to null eigenvalues and small negative ones becomes unclear without specific strategy. In order to highlight the efficiency of the approach presented in Section 5.3 we compare the singular values of the Schur complement with and without filtering mixed degrees of freedom from the condensation variables.

The graph based kernel detection methods are applied to the subdomains shown in Figure 16. The lumped weight is used for both methods and three damping values are considered $\alpha \in (0.3, 0.5, 0.9)$. Only four condensation nodes are used in this benchmark, leading to Schur complements \mathbf{S}_{cc} of size 20×20 when mixed degrees of freedom are not filtered out, and 12×12 otherwise.

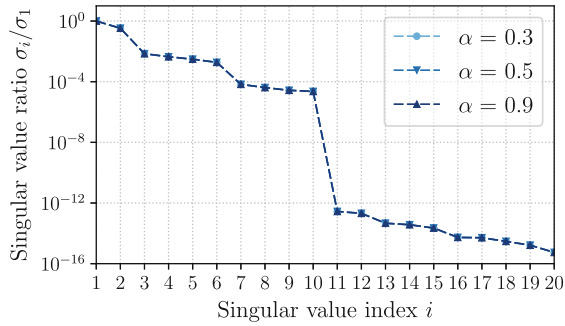
The singular values of the Schur complement selected by the Katz and Page Rank strategies applied to the floating subdomain are shown in Figure 18. Please note that in order to know in advance the inertia of the Schur complement, both the matrix and the inclusions are discretized with P2P1P1 elements. Pressure and volume discontinuities at the material interface are allowed. It is not a limitation of the method but it facilitates the analysis of the singular values. The inertia of the Schur complement is known *a priori* thanks to the Haynsworth additivity formula. When mixed degrees of freedom are not filtered out, 6 null eigenvalues and 4 (small) negative ones are expected. For both selection strategies, the detection process tends to identify 10 null singular values. The difference between singular values associated to null eigenvalues and small negative ones is totally blurred.



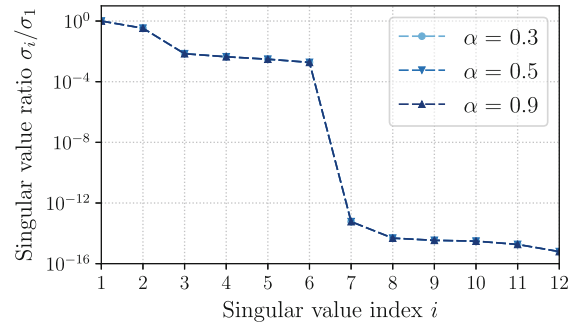
(A) Katz method for a floating subdomain.



(B) Katz method with mixed dof filter for a floating subdomain.

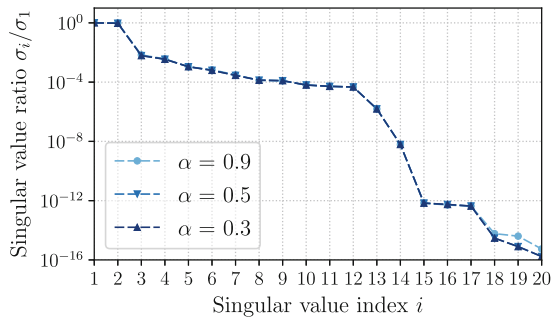


(C) Page Rank method for a floating subdomain.

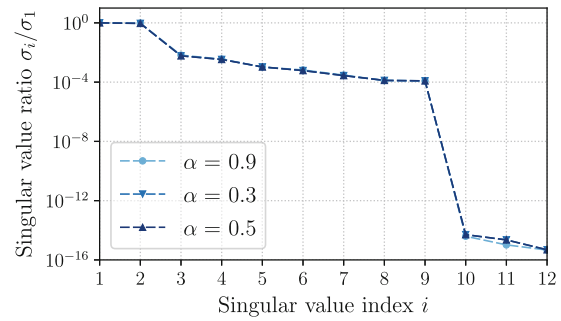


(D) Page Rank method with mixed dof filter for a floating subdomain.

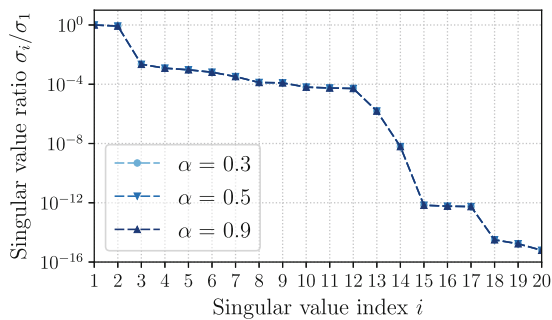
FIGURE 18 Solid propellant with P2P1P1 elements: Singular values of the Schur complement S_{cc} for Katz and Page Rank. Four condensation nodes are used with lumped weight



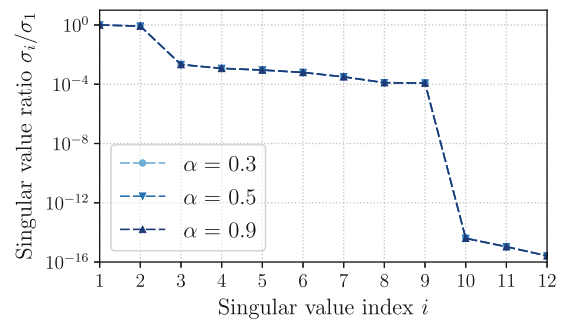
(A) Katz method for a partially constrained subdomain.



(B) Katz method with mixed dof filter for a partially constrained subdomain.



(C) Page Rank method for a partially constrained subdomain.



(D) Page Rank method with mixed dof filter for a partially constrained subdomain.

FIGURE 19 Solid propellant with P2P1P1 elements: Singular values of the Schur complement S_{cc} for Katz and Page Rank. Four condensation nodes are used with lumped weight

On the contrary, when mixed degrees of freedom are filtered out from the condensation variables, the positivity of the Schur complement is enforced and a clear distinction of null singular values is recovered.

The singular values of the Schur complement selected by the Katz and Page Rank strategies applied to the partially constrained subdomain are shown in Figure 19. Due to the boundary condition, 3 null eigenvalues are expected. Again, the filtering process of mixed degrees of freedom leads to a clear distinction of null singular values.

8 | CONCLUSIONS

This article has introduced a robust and affordable method to compute nullspace and generalized inverse of finite element operators involved in dual domain decomposition methods. It is a crucial point of the FETI methods since a misdetection of these kernels leads inevitably to the divergence of the iterative solver.

The methodology follows the fixing-node framework proposed in Brzobohatý et al.,³⁴ it relies on the operator partial factorization and on the analysis of a well chosen Schur complement. The selection process of fixing-nodes has been significantly improved to tackle ill conditioned problems. It makes use of graph centrality measures and consider weighted graphs to automatically pick good fixing-nodes candidates for heterogeneous problems. Eigenvector, Katz and Page Rank centralities are evaluated and compared with existing approaches. An extension to deal with symmetric indefinite systems arising from mixed finite elements is also presented.

The approach has been assessed on three academic but ill conditioned examples. A comparison with the MUMPS direct solver has been provided showing the good performance of the graph-based strategies. An industrial application is presented, the numerical homogenization of solid propellant. The effectiveness of the specific treatment of symmetric indefinite systems has been shown on this application.

Rather specific and often hidden under the hood, this robust process to compute nullspace and generalized inverse of floating subdomains is one of the key component to solve ill-conditioned problems with AMPFETI. It was used in all industrial applications shown in our previous published work, woven composite,⁶ non associated plasticity⁷ and high fidelity multiperforated aircraft combustion chamber involving thermomechanical loading and complex elastoplastic material.⁸

ACKNOWLEDGMENTS

The author would like to thanks P. Gosselet and A. Parret-Fréaud for fruitful discussions about the proposed work.

CONFLICT OF INTEREST

The authors declare no potential conflict of interests.

DATA AVAILABILITY STATEMENT

Data will be made available on request for the benchmarks presented in Section 6. The data that support the findings of this study are available from the corresponding author upon reasonable request.

ORCID

Christophe Bovet  <https://orcid.org/0000-0003-2390-0717>

REFERENCES

1. Farhat C, Roux FX. A method of finite element tearing and interconnecting and its parallel solution algorithm. *Int J Numer Methods Eng*. 1991;32(6):1205. doi:10.1002/nme.1620320604
2. Dostál Z, Horák D, Kučera R. Total FETI an easier implementable variant of the FETI method for numerical solution of elliptic PDE. *Commun Numer Methods Eng*. 2006;22(12):1155-1162. doi:10.1002/cnm.881
3. Kozubek T, Vondrák V, Menšík M, et al. Total FETI domain decomposition method and its massively parallel implementation. *Adv Eng Softw*. 2013;60-61:14-22. doi:10.1016/j.advengsoft.2013.04.001
4. Říha L, Brzobohatý T, Markopoulos A, Meca O, Kozubek T. Massively parallel hybrid total FETI (HTFETI) solver. Paper presented at: PASC'16, Association for Computing Machinery, New York, NY, USA; 2016.
5. Merta M, Říha L, Meca O, et al. Intel Xeon Phi acceleration of hybrid total FETI solver. *Adv Eng Softw*. 2017;112:124-135. doi:10.1016/j.advengsoft.2017.05.001
6. Bovet C, Parret-Fréaud A, Spillane N, Gosselet P. Adaptive multipreconditioned FETI: Scalability results and robustness assessment. *Comput Struct*. 2017;193:1-20. doi:10.1016/j.compstruc.2017.07.010

7. Bovet C, Gosselet P, Spillane N. Multipreconditioning for nonsymmetric problems: the case of orthomin and biCG. *Compt Rendus Math.* 2017;355(3):354-358. doi:10.1016/j.crma.2017.01.010
8. Bovet C, Parret-Fréaud A, Gosselet P. Two-level adaptation for Adaptive Multipreconditioned FETI. *Adv Eng Softw.* 2021;152:102952. doi:10.1016/j.advengsoft.2020.102952
9. Farhat C, Gérardin M. On the general solution by a direct method of a large-scale singular system of linear equations: application to the analysis of floating structures. *Int J Numer Methods Eng.* 1998;41(4):675-696. doi:10.1002/(SICI)1097-0207(19980228)41:4<675::AID-NME305>3.0.CO;2-8
10. Felippa CA, Park KC. The construction of free-free flexibility matrices for multilevel structural analysis. *Comput Methods Appl Mech Eng.* 2002;191(19):2139-2168. doi:10.1016/S0045-7825(01)00379-6
11. Toivanen J, Avery P, Farhat C. A multilevel FETI-DP method and its performance for problems with billions of degrees of freedom. *Int J Numer Methods Eng.* 2018;116(10-11):661-682. doi:10.1002/nme.5938
12. Brands D, Klawonn A, Rheinbach O, Schröder J. Modelling and convergence in arterial wall simulations using a parallel FETI solution strategy. *Comput. Methods Appl. Mech. Eng.* 2008;11(5):569-583.
13. Leistner MC, Gosselet P, Rixen DJ. Recycling of solution spaces in multi-preconditioned FETI methods applied to structural dynamics. *Int J Numer Methods Eng.* 2018;116. doi:10.1002/nme.5918
14. Dostál Z, Vlach O, Brzobohatý T. Scalable TFETI based algorithm with adaptive augmentation for contact problems with variationally consistent discretization of contact conditions. *Finite Elem Anal Des.* 2019;156:34-43. doi:10.1016/j.finel.2019.01.002
15. Bouclier R, Passieux JC. A domain coupling method for finite element digital image correlation with mechanical regularization: Application to multiscale measurements and parallel computing. *Int J Numer Methods Eng.* 2017;111(2):123-143. doi:10.1002/nme.5456
16. Klawonn A, Lanser M, Rheinbach O. Nonlinear FETI-DP and BDDC methods. *SIAM J Sci Comput.* 2014;36(2):A737-A765. Publisher: Society for Industrial and Applied Mathematics. doi:10.1137/130920563
17. Negrello C, Gosselet P, Rey C, Pebrel J. Substructured formulations of nonlinear structure problems – influence of the interface condition. *Int J Numer Methods Eng.* 2016;107(13):1083-1105. doi:10.1002/nme.5195
18. Kleiss SK, Pechstein C, Jüttler B, Tomar S. IETI – isogeometric tearing and interconnecting. *Comput Methods Appl Mech Eng.* 2012;247-248:201-215. doi:10.1016/j.cma.2012.08.007
19. Hirschler T, Bouclier R, Dureisseix D, Duval A, Elguedj T, Morlier J. A dual domain decomposition algorithm for the analysis of non-conforming isogeometric Kirchhoff–Love shells. *Comput Methods Appl Mech Eng.* 2019;357:112578. doi:10.1016/j.cma.2019.112578
20. Klawonn A, Rheinbach O. Robust FETI-DP methods for heterogeneous three dimensional elasticity problems. *Comput Methods Appl Mech Eng.* 2007;196(8):1400-1414. doi:10.1016/j.cma.2006.03.023
21. Klawonn A, Rheinbach O, Widlund OB. An analysis of a FETI-DP algorithm on irregular subdomains in the plane. *SIAM J. Numer. Anal.* 2008;46(5):2484-2504. doi:10.1137/070688675
22. Spillane N, Rixen DJ. Automatic spectral coarse spaces for robust FETI and BDD algorithms. *Int J Numer Methods Eng.* 2013;95(11):953-990. doi:10.1002/nme.4534
23. Mandel J, Sousedik B. Adaptive selection of face coarse degrees of freedom in the BDDC and the FETI-DP iterative substructuring methods. *Comput. Methods Appl. Mech. Eng.* 2007;196(8):1389-1399. doi:10.1016/j.cma.2006.03.010
24. Klawonn A, Kuhn M, Rheinbach O. Adaptive coarse spaces for FETI-DP in three dimensions. *SIAM J. Sci. Comput.* 2016;38(5):A2880-A2911. doi:10.1137/15M1049610
25. Heinlein A, Klawonn A, Lanser M, Weber J. Machine learning in adaptive domain decomposition methods—predicting the geometric location of constraints. *SIAM J Sci Comput.* 2019;41(6):A3887-A3912. doi:10.1137/18M1205364
26. Heinlein A, Klawonn A, Lanser M, Weber J. Combining machine learning and adaptive coarse spaces—a hybrid approach for robust FETI-DP methods in three dimensions. *SIAM J Sci Comput.* 2021;43(5):S816-S838. doi:10.1137/20M1344913
27. Klawonn A, Kühn MJ, Rheinbach O. Parallel adaptive FETI-DP using lightweight asynchronous dynamic load balancing. *Int J Numer Methods Eng.* 2020;121(4):621-643. doi:10.1002/nme.6237
28. Gosselet P, Rixen D, Roux FX, Spillane N. Simultaneous FETI and block FETI: robust domain decomposition with multiple search directions. *Int J Numer Methods Eng.* 2015;104(10):905-927. doi:10.1002/nme.4946
29. Bridson R, Greif C. A multipreconditioned conjugate gradient algorithm. *SIAM J. Matrix Anal. Appl.* 2006;27(4):1056-1068 (electronic). doi:10.1137/040620047
30. Spillane N. An adaptive multipreconditioned conjugate gradient algorithm. *SIAM J. Sci. Comput.* 2016;38(3):A1896-A1918. doi:10.1137/15M1028534
31. Molina R, Roux FX. New implementations for the Simultaneous-FETI method. *Int J Numer Methods Eng.* 2019;118(9):519-535. doi:10.1002/nme.6024
32. Papadrakakis M, Fragakis Y. An integrated geometric–algebraic method for solving semi-definite problems in structural mechanics. *Comput Methods Appl Mech Eng.* 2001;190(49–50):6513-6532. doi:10.1016/S0045-7825(01)00234-1
33. Dostál Z, Kozubek T, Markopoulos A, Menšík M. Cholesky decomposition of a positive semidefinite matrix with known kernel. *Appl Math Comput.* 2011;217(13):6067-6077. doi:10.1016/j.amc.2010.12.069
34. Brzobohatý T, Dostál Z, Kozubek T, Kovář P, Markopoulos A. Cholesky decomposition with fixing nodes to stable computation of a generalized inverse of the stiffness matrix of a floating structure. *Int J Numer Methods Eng.* 2011;88(5):493-509. doi:10.1002/nme.3187
35. Kučera R, Kozubek T, Markopoulos A, Machalová J. On the Moore–Penrose inverse in solving saddle-point systems with singular diagonal blocks. *Numer Linear Algebra Appl.* 2012;19(4):677-699. doi:10.1002/nla.798

36. Kučera R, Kozubek T, Markopoulos A. On large-scale generalized inverses in solving two-by-two block linear systems. *Linear Algebra Appl.* 2013;438(7):3011-3029. doi:10.1016/j.laa.2012.09.027
37. Mandel J. Balancing domain decomposition. *Commun Numer Methods Eng.* 1993;9(3):233. doi:10.1002/cnm.1640090307
38. Farhat C, Lesoinne M, LeTallec P, Pierson K, Rixen D. FETI-DP: a dual-primal unified FETI method - part i: a faster alternative to the two-level FETI method. *Int J Numer Methods Eng.* 2001;50(7):1523-1544. doi:10.1002/nme.76
39. Dohrmann CR. A preconditioner for substructuring based on constrained energy minimization. *SIAM J Sci Comput.* 2003;25:246. doi:10.1137/s1064827502412887
40. Golub GH, Loan CFV. *Matrix Computations*. JHU Press; 2012.
41. Newman MEJ. *Networks*. second ed. Oxford University Press; 2018.
42. Amestoy PR, Duff IS, Koster J, L'Excellent JY. A fully asynchronous multifrontal solver using distributed dynamic scheduling. *SIAM J Matrix Anal Appl.* 2001;23(1):15-41. doi:10.1137/S0895479899358194
43. Suzuki A, Roux FX. A dissection solver with kernel detection for symmetric finite element matrices on shared memory computers. *Int J Numer Methods Eng.* 2014;100(2):136-164. doi:10.1002/nme.4729
44. Lorentz E. A mixed interface finite element for cohesive zone models. *Comput Methods Appl Mech Eng.* 2008;198(2):302-317. doi:10.1016/j.cma.2008.08.006
45. Zienkiewicz OC, Taylor RL, Fox D. *The Finite Element Method for Solid and Structural Mechanics*. 7th ed. Elsevier/Butterworth-Heinemann; 2014.
46. Kabelíková P. Graph centers used for stabilization of matrix factorizations. *Discuss Math Graph Theory.* 2010;30(2):249-259.
47. Kabelíková P. *Implementation of Non-Overlapping Domain Decomposition Techniques for FETI Methods*. PhD thesis. VSB – Technical University of Ostrava, Faculty of Electrical Engineering and Computer Science Department of Applied Mathematics; 2012.
48. Briggs WL, Henson VE, McCormick SF. *A Multigrid Tutorial*. 2nd ed. Society for Industrial and Applied Mathematics; 2000.
49. Markopoulos A, Říha L, Brzobohatý T, et al. Treatment of singular matrices in the hybrid total FETI method. In: Lee CO, Cai XC, Keyes DE, et al., eds. *Domain Decomposition Methods in Science and Engineering XXIII*. Springer International Publishing; 2017:237-244.
50. Katz L. A new status index derived from sociometric analysis. *Psychometrika.* 1953;18(1):39-43. doi:10.1007/BF02289026
51. Brin S, Page L. The anatomy of a large-scale hypertextual Web search engine. *Comput Netw ISDN Syst.* 1998;30(1-7):107-117. doi:10.1016/S0169-7552(98)00110-X
52. Hruskova P. Analysis of fixing nodes used in generalized inverse computation. *Adv Electr Electron Eng.* 2014;12(2):123-130. doi:10.15598/aeer.v12i2.1020
53. Brezzi F, Fortin M. *Mixed and Hybrid Finite Element Methods*. Springer Series in Computational Mathematics. Vol 15. Springer; 1991.
54. Zhang F. *The Schur Complement and Its Applications*. Numerical Methods and Algorithms. Vol 4. 1st ed. Springer-Verlag; 2005.
55. Pellegrini F. *Scotch and PT-Scotch Graph Partitioning Software: An Overview*. Chapman and Hall/CRC; 2012.
56. Gosselet P, Rey C. Non-overlapping domain decomposition methods in structural mechanics. *Arch Comput Methods Eng.* 2006;13(4):515-572. doi:10.1007/BF02905857

How to cite this article: Bovet C. On the use of graph centralities to compute generalized inverse of singular finite element operators: Applications to the analysis of floating substructures. *Int J Numer Methods Eng.* 2023;1-32. doi: 10.1002/nme.7193